JM PAPERS

Wave propagation in random two-dimensional turbulence: a multiscale approach

Valentin Resseguier[1,2,†]**, Erwan Hascoët**[3] **and Bertrand Chapron**[4,5]

[1]UR OPAALE, INRAE, 17 avenue de Cucillé, F-35044 Rennes, France

[2]LAB, SCALIAN DS, 2 Rue Antoine Becquerel, 35700 Rennes, France

[3]Oceandatalab, 870 Rte de Deolen, 29280 Locmaria-Plouzané, France

[4]Univ Brest, Ifremer, CNRS, IRD, LOPS, F-29280 Plouzané, France

[5]Ifremer, INRIA, ODYSSEY, F-29280 Plouzané, France

To study two-dimensional dispersive waves propagating through turbulent flows, a new and less restrictive fast waves approximation is proposed using a multiscale setting. In this ansatz, large and small scales of the turbulence are treated differently. Correlation lengths of the random small-scale turbulence components can be considered negligible in the wave packet propagating frame. Nevertheless, the large-scale flow can be relatively strong, to significantly impact wavenumbers along the propagating rays. New theoretical results, numerical tools and proxies are derived to describe ray and wave action distributions. All model parameters can be calibrated robustly from the large-scale flow component only. We illustrate our purpose with ocean surface gravity waves propagating in different types of surface currents. The multiscale solution is demonstrated to efficiently document wave trapping effects by intense jets.

1. Introduction

This paper aims to revisit the ray path concept for fast waves propagating over heterogeneous turbulent flows. Considering ocean surface wave propagation, many authors have already discussed the random changes of rays subject to a random current (Voronovich 1991; White & Fornberg 1998; Smit & Janssen 2019), and consequences on wave action distributions. Closures have been derived in the Eulerian setting (Bal & Chou 2002; Klyatskin & Koshel 2015; Borcea, Garnier & Solna 2019; Kafiabad, Savva & Vanneste 2019; Bôas & Young 2020; Garnier, Gay & Savin 2020). Some of

† Email address for correspondence: valentin.resseguier@inrae.fr

these approaches can be traced back to wave–wave interaction models (e.g. McComas & Bretherton (1977); see also Kafiabad *et al.* (2019), and references therein). In most cases, the central assumption is either time-delta-correlated turbulent velocity (Voronovich 1991; Klyatskin 2005; Klyatskin & Koshel 2015) and/or fast waves in comparison to fluid flow velocities (White & Fornberg 1998; Dysthe 2001; Bal & Chou 2002; Borcea *et al.* 2019; Kafiabad *et al.* 2019; Smit & Janssen 2019; Bôas & Young 2020; Garnier *et al.* 2020; Boury, Bühler & Shatah 2023; Wang *et al.* 2023). Medium variations may be slow, and delta-correlations are hardly justifiable in a fixed frame. However, attached to a fast-propagating wave group, the medium may seem to vary rapidly, and the delta-correlation assumption makes more sense. Another common assumption is frozen turbulence. In such a case, weak currents also imply conservation along rays of intrinsic frequency, wavenumber and group velocity magnitude in two dimensions (Boury *et al.* 2023). Subsequently, most wave dynamics models neglect variations and diffusion of frequency or wavenumber.

The diffusion of the wave action at large distance with a multiscale decomposition of the current has already been reported (Bal & Chou 2002). However, an explicit formulation for the diffusivity has been derived solely for a zero large-scale current. More generally, fast wave models rely mostly on either zero or constant current components at larger scales. West (1978), for instance, discussed acoustic waves in two-component random media, but no velocity was involved.

Hereafter, the proposed two-scale velocity decomposition falls into the family of stochastic transport models (Kunita 1997; Mikulevicius & Rozovskii 2004; Resseguier *et al.* 2020*a*; Zhen, Resseguier & Chapron 2023), including dynamics under location uncertainty (LU) (Mémin 2014; Resseguier, Mémin & Chapron 2017*a*) and stochastic advection by Lie transport (SALT) (Holm 2015). Under this framework, the small-scale velocity component is delta-correlated in time (Cotter, Gottwald & Holm 2017). Up to usual source terms, fluid dynamics quantities (temperature, momentum, etc.) are transported by both the large-scale revolved component and that random unresolved turbulence component. The stochastic closures obtained are conservative. Nonlinear wave Hamiltonian dynamics and wave influence on currents (e.g. Stokes drift) have then been derived (e.g. Crisan & Holm 2018; Bauer *et al.* 2020; Holm 2021; Holm & Luesink 2021; Dinvay & Mémin 2022; Holm, Hu & Street 2023). Considering a single-wavevector current, solutions for a monochromatic shallow-water wave were developed by Mémin *et al.* (2022). In the present study, our objective is restricted to the influence of turbulent flows on linear waves.

After first recalling the principles of the ray tracing method, we present the multiscale framework for fast wave dynamics, its physical grounds, and a calibration method for the closure. Simplified stochastic equations are then derived for the ray dynamics and the wave action spectrum, in both Lagrangian and Eulerian settings. For illustrative examples, numerical tools, analytic models and proxies are applied to ocean surface gravity waves propagating through two types of two-dimensional (2-D) turbulent flows: a typical slow homogeneous turbulence, and a jet case.

2. Characteristics of wave packet rays

Isolating a single progressive group of quasi-regular wave trains, it follows a form $h(\boldsymbol{x}, t) \exp(\mathrm{i}\phi(\boldsymbol{x}, t)) + \text{c.c.}$, for most properties. Typically, h would be the local wave height, in metres. If a packet is to be followed, then the phase $\phi(\boldsymbol{x}, t)$ must vary smoothly along the propagation, i.e. $\phi(\boldsymbol{x}, t)$ is differentiable. The relative frequency is then

$\omega = -\partial_t \phi(x, t)$, and the wavenumber vector is $k = \nabla \phi(x, t)$, with wavenumber $k = \|k\|$, and direction given by the normalized wavevector, $\tilde{k} = k/k = \begin{pmatrix} \cos \theta_k \\ \sin \theta_k \end{pmatrix}$. To first order, such a train of waves is dispersive, and the intrinsic frequency reads

$$\omega - k \cdot v = \omega_0 = \begin{cases} \text{constant} \times \dfrac{1}{\alpha} k^\alpha, & \alpha \neq 0, \\ \text{constant} \times \log(k), & \alpha = 0, \end{cases} \tag{2.1}$$

and propagates with its group velocity $v_g = \nabla_k \omega$, constantly modified by the local velocity of the currents v,

$$\frac{dx_r}{dt} = v_g = v_g^0 + v, \tag{2.2}$$

where x_r is the centroid of a wave group, $v_g^0 = (\partial \omega_0(k)/\partial k)\, \tilde{k}$ is the group velocity without currents, i.e. depending solely on the wavevector. For $\alpha = 1$, the medium is non-dispersive (e.g. acoustic waves). Parameter $\alpha = 1/2$ corresponds to gravity waves over deep ocean ($\omega_0 = \sqrt{gk}$). The dominant wavevector k within the group evolves according to

$$\frac{dk}{dt} = -\nabla v^{\mathrm{T}} k. \tag{2.3}$$

Equations (2.2)–(2.3) are the Hamilton eikonal equations. Along the propagating ray, velocity gradients induce linear variations. Decelerating currents will, for instance, shorten waves, and reduce the group velocity. Travelling over fields of random velocities v, the wavevector k will also become randomly distributed. Scattering of ocean surface wave packets by random currents can generally be assumed to be weak, with $\|v\|$ of order $0.5\,\mathrm{m\,s}^{-1}$, much smaller than $v_g^0 = \|v_g^0\|$ of order $10\,\mathrm{m\,s}^{-1}$. Yet cumulative effects of these random surface currents can lead to strong convergence or divergence between initially nearby ray trajectories.

To complete the wave field description, $E(x, t) = \frac{1}{2}\rho g h^2(x, t)$ and $A(x, t) = E(x, t)/\omega_0(k(x, t))$ denote energy and action by unit of surface. Here, E is expressed in $\mathrm{J\,m}^{-2}$, and A in $\mathrm{J\,s\,m}^{-2}$. To avoid spurious notations, we set the multiplicative constant $\frac{1}{2}\rho g$ to unity. The wave action is considered to be an adiabatic invariant in the absence of source terms. Wave action is then crucial to anticipate wave transformations by currents (White 1999). Unlike wave energy, wave action is conserved, in the absence of wave generation or dissipation. This action is the integral over wavevectors of the action spectrum N, also related to the wave energy spectrum E:

$$A(x, t) = \int dk\, N(x, k, t) = \int dk\, \frac{E(x, k, t)}{\omega_0(k, t)}. \tag{2.4}$$

Action and energy spectrum quantify action and energy by unit of surface (unit of x) and by unit of wavevector surface (unit of k). Consider the (x, k) variable change between different times t_i and t_f integrating the characteristic eikonal equations (2.2)–(2.3):

$$\begin{pmatrix} x_r(t_i) \\ k(t_i) \end{pmatrix} \mapsto \begin{pmatrix} x_r(t_f) \\ k(t_f) \end{pmatrix}. \tag{2.5}$$

According to the Liouville theorem for Hamiltonian mechanics (Landau & Lifshitz 1960, § 46), the state space of the 'packet-by-packet' approach (the (x, k) space) does not

contract or dilate along time. Readers not familiar with Hamiltonian dynamics may see the divergence free of the four-dimensional flow (2.5) – i.e. $\nabla_{\boldsymbol{x}} \cdot \mathrm{d}\boldsymbol{x}_r/\mathrm{d}t + \nabla_{\boldsymbol{k}} \cdot \mathrm{d}\boldsymbol{k}/\mathrm{d}t = 0$ – as the divergence free of incompressible flow velocities, leading naturally to volume-preserving dynamics. Therefore, if wave dissipation is neglected, then the wave action spectrum N is conserved (Lavrenov 2013), i.e.

$$N(\boldsymbol{x}_r(t_i), \boldsymbol{k}(t_i), t_i) = N(\boldsymbol{x}_r(t_f), \boldsymbol{k}(t_f), t_f). \tag{2.6}$$

This result is extremely useful because it involves only quantities of the characteristics, i.e. each Fourier mode can be modified independently of the others. The wave energy spectrum can be computed from the characteristics

$$E(\boldsymbol{x}_r(t_f), \boldsymbol{k}(t_f), t_f) = \frac{\omega_0(\boldsymbol{k}(t_f))}{\omega_0(\boldsymbol{k}(t_i))} E(\boldsymbol{x}_r(t_i), \boldsymbol{k}(t_i), t_i). \tag{2.7}$$

starting with an initial incoming wave spectrum $E(\boldsymbol{x}_r(t_i), \boldsymbol{k}(t_i), t_i)$ for every wavevector $\boldsymbol{k}(t_i)$, starting from a small set of spatial points $\boldsymbol{x}_r(t_i)$.

3. A new fast wave assumption

Eikonal equations (2.2)–(2.3) are driven by currents and their gradients. Commonly, the Eulerian current $\boldsymbol{v}$ is decomposed into a low-frequency large-scale component $\bar{\boldsymbol{v}}$ and a transient small-scale unresolved component $\boldsymbol{v}'$:

$$\boldsymbol{v} = \bar{\boldsymbol{v}} + \boldsymbol{v}'. \tag{3.1}$$

Current gradients naturally follow the same scale separation. From now on, we will consider divergence-free 2-D currents only.

3.1. *The ray Lagrangian correlation time*

To better characterize the wave dynamics in such a random environment, the covariance of the fluid velocity can be evaluated in the wave group frame. To take into account the small-scale unresolved component $\boldsymbol{v}'$, its Eulerian spatio-temporal covariance is considered, assuming statistical homogeneity and stationarity for the Eulerian velocity $\boldsymbol{v}'_E(t, \boldsymbol{x}) = \boldsymbol{v}'(t, \boldsymbol{x})$:

$$C_{ij}^{v'_E}(\delta t, \delta \boldsymbol{x}) = \mathbb{E}(v'_i(t, \boldsymbol{x}) \, v'_j(t + \delta t, \boldsymbol{x} + \delta \boldsymbol{x})) = \mathbb{E}(v'_i(t, \boldsymbol{x}_r(t)) \, v'_j(t + \delta t, \boldsymbol{x}_r(t) + \delta \boldsymbol{x})), \tag{3.2}$$

where $\boldsymbol{x}_r$ is a solution of (2.2) with an arbitrary initial position $\boldsymbol{x}_r^0$. Then we define $v'_R(t) = v'(t, \boldsymbol{x}_r(t))$, the Lagrangian velocity along the ray $\boldsymbol{x}_r(t)$. The temporal covariance of the small-scale component $\boldsymbol{v}'$ – in the wave group frame – is the covariance of that Lagrangian velocity:

$$C_{ij}^{v'_R}(\delta t) = \mathbb{E}(v'_i(t, \boldsymbol{x}_r(t)) \, v'_j(t + \delta t, \boldsymbol{x}_r(t + \delta t))) = C_{ij}^{v'_E}(\delta t, \boldsymbol{x}_r(t + \delta t) - \boldsymbol{x}_r(t)). \tag{3.3}$$

Assuming, for example, a typical isotropic form for the Eulerian covariance,

$$C^{v'_E}(\delta t, \delta \boldsymbol{x}) = C\left(\frac{|\delta t|}{\tau_{v'}} + \frac{\|\delta \boldsymbol{x}\|}{l_{v'}}\right), \tag{3.4}$$

the covariance can be evaluated in the wave group frame for small time increment δt:

$$C^{v'_R}(\delta t) = C\left(\frac{|\delta t|}{\tau_{v'}} + \frac{\|x_r(t'+t) - x_r(t')\|}{l_{v'}}\right) = C\left(\left(\frac{1}{\tau_{v'}} + \frac{\|v_g\|}{l_{v'}}\right)|\delta t| + O(\delta t^2)\right),$$
(3.5)

since $x_r(t'+t) - x_r(t') = v_g\,\delta t + O(\delta t^2)$. Therefore, $(1/\tau_{v'} + \|v_g\|/l_{v'})^{-1}$ is the correlation time of $v'(t, x_r(t))$. For fast waves, the along-ray correlation time of the small-scale velocity can be approximated by $l_{v'}/v_g^0$. Note that eikonal equations (2.2)–(2.3) involve both velocity and velocity gradients. The above derivation is also valid for the small-scale velocity gradients $(\nabla v^{\mathrm{T}})'(t, x_r(t))$. The ratio ϵ between that along-ray correlation time and the characteristic time of the wave group properties evolution will then control the time decorrelation assumption of v':

$$\epsilon = \frac{l_{v'}}{v_g^0}\,\|\nabla v^{\mathrm{T}}\| \sim \frac{l_{v'}}{l_v}\,\frac{\|v\|}{v_g^0}.$$
(3.6)

This time scale estimation can be obtained from spatio-temporal covariances more general than (3.4) (not shown) even though the derivation is more technical. Note that the Eulerian small-scale velocity v' is not necessarily time-uncorrelated, as assumed in Voronovich (1991) and Klyatskin & Koshel (2015). Yet for small enough ϵ, the Lagrangian small-scale velocity along the ray can be considered time-uncorrelated. From the expression for ϵ, such a condition depends upon:

  (i) v_g^0, the fast wave group velocity;
 (ii) $\|v\|$, often slow but not always negligible compared to the intrinsic wave group v_g^0;
(iii) $l_{v'}/l_v$, related to the separation between large scales $\bar{v}$ and small scales v', e.g. the spatial filtering cutoff of the large-scale velocity $\bar{v}$, but also related to its kinetic energy distribution over spatial scales, typically the spectrum slope.

This along-ray partial time-decorrelation assumption is less restrictive than the usual fast wave approximation (White & Fornberg 1998; Dysthe 2001; Bal & Chou 2002; Borcea *et al.* 2019; Kafiabad *et al.* 2019; Smit & Janssen 2019; Bôas & Young 2020; Garnier *et al.* 2020; Boury *et al.* 2023; Wang *et al.* 2023) – say $\|v\|/v_g^0 \ll 1$ – and than the SALT-LU time-decorrelation used for turbulence dynamics (Mémin 2014; Holm 2015; Cotter *et al.* 2017; Resseguier *et al.* 2020a) – say $l_{v'}/l_v \ll 1$. Similarly, this last validity criterion can be obtained by replacing x_r in (3.2)–(3.6) by the fluid particle Lagrangian path x (solution of $\mathrm{d}x/\mathrm{d}t = v$) and thus v_g^0 by v. These asymptotic models often rely on averaging or homogenization techniques (Papanicolaou & Kohler 1974; White & Fornberg 1998) to derive Markovian dynamics involving various types of diffusivity.

3.2. *Ray absolute diffusivity and turbulence statistics: calibration*

Diffusivity is a natural tool to specify statistics of uncorrelated random media. For waves in random media, we will specify multi-point statistics, and the Fourier space is convenient for this purpose. We will first present scalar diffusivity and then distribute it over spatial scales to fully calibrate the random velocity v', i.e. choose some parameter values to set the statistics of that velocity field. As such, we will obtain a closed model to derive analytic results and generate samples for simulations.

The absolute diffusivity (or Kubo-type formula) usually corresponds, in the so-called diffusive regime, to the variance per unit of time of a fluid particle Lagrangian path

$\mathrm{d}\boldsymbol{x}(t)/\mathrm{d}t = \boldsymbol{v}_L(t) = \boldsymbol{v}(t, \boldsymbol{x}(t))$. It is approximately equal to the velocity variance times its correlation time. The Eulerian velocity covariance (3.4) will thus induce an absolute diffusivity (Piterbarg & Ostrovskii 1997; Klyatskin 2005)

$$\frac{1}{2} a^L = \int_0^{+\infty} \mathrm{d}\delta t \, C^{v'_L}(\delta t) = \int_0^{+\infty} \mathrm{d}\delta t \, C^{v'_E}(\delta t, \boldsymbol{x}(t+\delta t) - \boldsymbol{x}(t)) \approx \frac{1}{2} \tau_{v'} C(0). \quad (3.7)$$

This diffusivity well describes effects of fast-varying eddies, but is not appropriate in our case. Indeed, along a propagating wave group $\mathrm{d}\boldsymbol{x}_r(t)/\mathrm{d}t = \boldsymbol{v}_g^0(t) + \boldsymbol{v}_R(t)$, a ray absolute diffusivity occurs and slightly differs from the usual absolute diffusivity to become

$$\frac{1}{2} a^R = \int_0^{+\infty} \mathrm{d}\delta t \, C^{v'_R}(\delta t) \approx \frac{1}{2} \left(\frac{1}{\tau_{v'}} + \frac{\|\boldsymbol{v}_g\|}{l_{v'}} \right)^{-1} C(0) \approx \frac{1}{2} \frac{l_{v'}}{v_g^0} C(0). \quad (3.8)$$

The absolute diffusivity sets the amplitude of the small-scale velocity $\boldsymbol{v}'$. Indeed, since the kinetic energy of a time-continuous white noise is infinite, it has no physical meaning. It is more relevant to deal with absolute diffusivity rather than kinetic energy in order to describe the statistics of the time-uncorrelated velocity. To calibrate its spatial correlations, we may focus on its Fourier transform $\widehat{\boldsymbol{v}'}(\boldsymbol{\kappa}, t)$, denoting by $\boldsymbol{\kappa} = \kappa \begin{pmatrix} \cos\theta_\kappa \\ \sin\theta_\kappa \end{pmatrix}$, the surface current wavevector. By analogy with the current kinetic energy spectra $E_\kappa = \frac{1}{2} \oint_0^{2\pi} \mathrm{d}\theta_\kappa \, \kappa (\|\hat{\boldsymbol{v}}(\boldsymbol{\kappa}, t)\|^2/(2\pi)^2)$, Resseguier, Mémin & Chapron (2017b) and Resseguier, Pan & Fox-Kemper (2020b) decompose the absolute diffusivity scale by scale:

$$a^R = \int_0^{+\infty} A_{v'}^R(\kappa) \, \mathrm{d}\kappa. \quad (3.9)$$

Referring it to absolute diffusivity spectral density (ADSD), it is defined as the kinetic energy spectra multiplied by the correlation time at each scale, $\tau(\kappa)$. Unlike Resseguier *et al.* (2017b, 2020b), that correlation time is here imposed by the wave dynamics. Therefore, by analogy with (3.8), we choose a correlation time $\tau^R(\kappa) = 1/\kappa/v_g^0(k)$, and then

$$\frac{1}{2} A^R(\kappa) = \frac{1}{2} \tau^R(\kappa) E_\kappa(\kappa) = \frac{1}{2} \frac{1/\kappa}{v_g^0(k)} E_\kappa(\kappa), \quad (3.10)$$

where k denotes the wave wavenumber and κ the current wavenumber.

To calibrate an equivalent noise, we model $\boldsymbol{v}'$ by $\boldsymbol{\sigma} \, \mathrm{d}B_t/\mathrm{d}t$, where $\mathrm{d}B_t/\mathrm{d}t$ is a spatio-temporal white noise, and $\boldsymbol{\sigma}$ denotes a spatial filtering operator that encodes spatial correlations through its ADSD, $A_{v'}^R$ and the horizontal incompressibility condition ($\nabla \cdot \boldsymbol{\sigma} = 0$). For incompressibility, we work with the curl of a streamfunction. To generate a homogeneous and isotropic streamfunction, we can filter a one-dimensional white noise $\dot{B}$ with a filter $\breve{\psi}_\sigma$ (Resseguier *et al.* 2017b), i.e. $\breve{\psi}_\sigma \star \dot{B}$, where $\star$ denotes a spatial convolution. The velocity field is hence

$$\boldsymbol{v}' = \boldsymbol{\sigma} \, \mathrm{d}B_t/\mathrm{d}t = \nabla^\perp \breve{\psi}_\sigma \star \mathrm{d}B_t/\mathrm{d}t, \quad (3.11)$$

with $\nabla^\perp$ the 2-D curl. That formula is easily written and implementable in Fourier space (see (A2)). To define the streamfunction filter, we note that $(\pi\kappa^3/(2\pi)^2)|\widehat{\breve{\psi}}_\sigma(\kappa)|^2 = \frac{1}{2} \oint_0^{2\pi} \mathrm{d}\theta_\kappa \, \kappa (\|\widehat{\boldsymbol{\sigma} \, \mathrm{d}B_t}(\boldsymbol{\kappa})\|^2/(2\pi)^2 \, \mathrm{d}t) = A_{v'}^R(\kappa)$, i.e. the filter can

997 A51-6
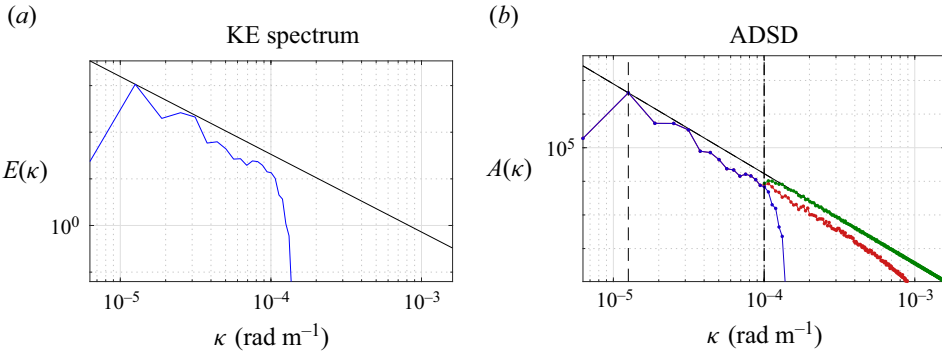
Figure 1. (*a*) Kinetic energy (KE) spectrum ($m^2\,s^{-2}/\,(rad\,m^{-1})$) and (*b*) ADSD ($m^2\,s^{-1}/\,(rad\,m^{-1})$) of the resolved high-resolution velocity A^R in red, low-resolution velocity $A_{\bar{v}}^R$ in blue, and modelled stochastic velocity $A_{v'}^R(\kappa) = A_0^R \kappa^{-\mu} - A_{\bar{v}}^R(\kappa)$ in green. For the ADSD power law $A^R(\kappa) \approx A_0^R \kappa^{-\mu}$, we impose the theoretical kinetic energy spectrum slope $-\frac{5}{3}$ (black solid line), coherently with homogeneous surface quasi-geostrophic dynamics (see § 5). The residual ADSD (green line) is set to extrapolate that power law at small scales.

be fully defined by the small-scale ADSD $A_{v'}^R$. To close our model, we assume an ADSD power law:

$$A^R(\kappa) \approx A_0^R \kappa^{-\mu}. \tag{3.12}$$

It enables automatic closure calibration $A_{v'}^R(\kappa) = A_0^R \kappa^{-\mu} - A_{\bar{v}}^R(\kappa)$, from instantaneous large-scale current statistics $A_{\bar{v}}^R$ only (Resseguier *et al.* 2020*b*), as illustrated in figure 1.

4. Statistical wave dynamics

In a stochastic framework, the Stratonovich or Itō notations can both be used (Kunita 1997; Oksendal 1998). Under Stratonovich calculus rules, expressions become similar to deterministic ones. Specifically, stochastic versions of linearized dynamical equations are obtained by replacing $\boldsymbol{v}$ by $\bar{\boldsymbol{v}} + \boldsymbol{\sigma} \circ dB_t/dt$. Then the stochastic transport of phase $(d\phi/dt) = \omega_0(\|\nabla\phi\|)$, i.e. – up to that velocity replacement – the Stratonovich dispersion relation, is exactly (2.1). The method of characteristics also applies. Note that one can switch from Stratonovich to Itō notations, where $\boldsymbol{v}'$ corresponds to $\boldsymbol{\sigma}\,dB_t/dt$. The characteristics equations (2.2)–(2.3) also remain unchanged for homogeneous and isotropic $\boldsymbol{v}'$:

$$\begin{cases} d\boldsymbol{x}_r = (\boldsymbol{v}_g^0 + \bar{\boldsymbol{v}})\,dt + \boldsymbol{\sigma}\,dB_t, \\ d\boldsymbol{k} = -\nabla(\bar{\boldsymbol{v}}\,dt + \boldsymbol{\sigma}\,dB_t)^T \boldsymbol{k}. \end{cases} \tag{4.1}$$

4.1. *Single-ray stochastic differential equations*

When studying a single ray in a homogeneous and isotropic turbulence (3.11), the wavevector dynamics simplifies. In the local crest-oriented frame, the influence of small-scale currents can be represented solely by four one-dimensional white noise forcings.

Notably, dynamics of wavevectors (2.3) are similar to tracer gradient dynamics (Bühler 2009; Plougonven & Zhang 2014). Only the coupled ray path dynamics (2.2) differs. Accordingly, we follow the notations and derivations of the mixing analysis from Lapeyre,
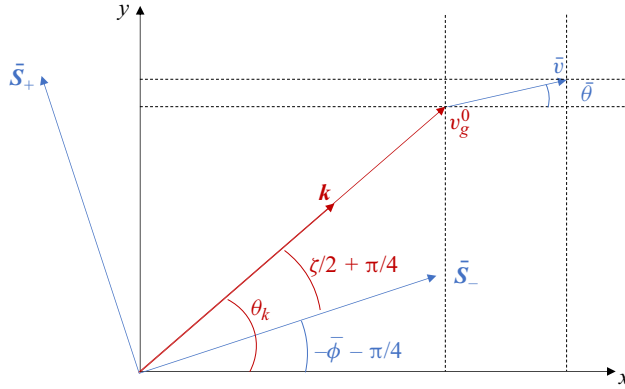
Figure 2. Schematic view of vectors and angles involved in single-ray dynamics, where $\bar{S}_-$ and $\bar{S}_+$ are respectively compression and dilatation axes associated with the large-scale velocity gradient $\boldsymbol{\nabla}\bar{\boldsymbol{v}}^{\mathrm{T}}$.

Klein & Hua (1999), and references therein. Without loss of generality, the large-scale velocity can be parametrized as

$$\bar{\boldsymbol{v}} = \bar{v}\begin{pmatrix}\cos\bar{\theta}\\\sin\bar{\theta}\end{pmatrix} \quad \text{and} \quad \boldsymbol{\nabla}\bar{\boldsymbol{v}}^{\mathrm{T}} = \frac{1}{2}\begin{bmatrix}\bar{\sigma}\sin 2\bar{\phi} & \bar{\omega}+\bar{\sigma}\cos 2\bar{\phi}\\-\bar{\omega}+\bar{\sigma}\cos 2\bar{\phi} & -\bar{\sigma}\sin 2\bar{\phi}\end{bmatrix}. \tag{4.2a,b}$$

Figure 2 provides a synthetic view of angles involved. The dynamics wave group centroid $\boldsymbol{x}_r$ is driven directly by the large current wave group velocity $\boldsymbol{v}_g^0 + \bar{\boldsymbol{v}}$. The influence of the large-scalecurrent gradients on the wavevector dynamics (4.1), expressed in the local crest-oriented frame $(\tilde{\boldsymbol{k}}, \tilde{\boldsymbol{k}}^\perp)$, is straightforward (Lapeyre *et al.* 1999). The small-scale currents force the ray dynamics through a stochastic noise. For a single ray $(\boldsymbol{x}_r, \boldsymbol{k}) = (x_r, y_r, k\cos\theta_k, k\sin\theta_k)$, this noise can be described rigorously by four independent one-dimensional white noises only (see Appendix A), $\dot{B}_t^{(1)}$, $\dot{B}_t^{(2)}$, $\dot{B}_t^{(3)}$ and $\dot{B}_t^{(4)}$, and

$$\frac{\mathrm{d}}{\mathrm{d}t}x_r = v_g^0\cos\theta_k + \bar{v}\cos\bar{\theta} + \sqrt{a_0}\,\dot{B}_t^{(1)}, \tag{4.3}$$

$$\frac{\mathrm{d}}{\mathrm{d}t}y_r = v_g^0\sin\theta_k + \bar{v}\sin\bar{\theta} + \sqrt{a_0}\,\dot{B}_t^{(2)}, \tag{4.4}$$

$$\frac{\mathrm{d}}{\mathrm{d}t}\log k = -\bar{\sigma}\sin(\zeta) + \gamma_0 + \sqrt{\gamma_0}\,\dot{B}_t^{(3)}, \tag{4.5}$$

$$\frac{\mathrm{d}}{\mathrm{d}t}\theta_k = \frac{1}{2}(\bar{\omega}-\bar{\sigma}\cos(\zeta)) + \sqrt{3\gamma_0}\,\dot{B}_t^{(4)}, \tag{4.6}$$

where $\zeta = 2(\theta_k + \bar{\phi})$ and

$$a_0 = \frac{1}{2\,\mathrm{d}t}\mathbb{E}\|\boldsymbol{\sigma}\,\mathrm{d}B_t\|^2 = \int_0^{+\infty}A_{v'}^R(\kappa)\,\mathrm{d}\kappa, \tag{4.7}$$

$$\gamma_0 = \frac{1}{8\,\mathrm{d}t}\mathbb{E}\|\boldsymbol{\nabla}_x(\boldsymbol{\sigma}\,\mathrm{d}B_t)^{\mathrm{T}}\|^2 = \frac{1}{4}\int_0^{+\infty}k^2\,A_{v'}^R(\kappa)\,\mathrm{d}\kappa. \tag{4.8}$$

Diffusivity constants depend through (3.10) on both the correlation length and the spectrum slope of the small-scale velocity. In contrast to the classical fast wave

approximation, the wavenumber does vary. This is due to (i) the finite large-scale strain rate $\bar{\sigma}$, and (ii) the small-scale isotropic velocity model (3.11). This isotropy assumption and its implication are discussed in Appendix C. Note that neither the large-scale component nor the small-scale component is assumed to be steady, even though that Eulerian velocity unsteadiness is only a secondary process in the wave dynamics. The fast temporal variations seen by the wave are driven mainly by the large wave speed and not by the Eulerian velocity unsteadiness. The current unsteadiness can also lead to wavenumber variations (Dong, Bühler & Smith 2020; Boury *et al.* 2023; Cox, Kafiabad & Vanneste 2023). Given a known wavevector angle, it leads to a wavenumber evolution

$$k(t) = k(0) \exp\left(-\int_0^t \bar{\sigma}\sin(2(\theta_k + \bar{\phi}))\,\mathrm{d}t'\right) \exp(\gamma_0 t + \sqrt{\gamma_0}\,B_t^{(3)}), \tag{4.9}$$

and hence to the complete wavevector distribution, i.e. the wave spectrum. The second exponential factor in (4.9) is a geometric Brownian motion. Its mean diverges in time exponentially rapidly. Physically, shear and strain of $\boldsymbol{v}'$ tends to shorten the wavelength (Voronovich 1991; Boury *et al.* 2023) leading to this exponential divergence. This factor has a log-normal distribution, suggesting possible extreme transient wavenumber events. This generalizes previous results (Voronovich 1991; Klyatskin & Koshel 2015), obtained with neglecting the time-correlated current component $\bar{\boldsymbol{v}}$.

For completeness, the action distribution over space and wavevector can be derived. Some approaches consider finite-size wave trains either through additional equations (Jonsson 1990; White & Fornberg 1998) or re-meshing (Hell, Fox-Kemper & Chapron submitted). Otherwise, each ray transports its action spectrum (2.6), and we need to numerically combine many rays (Lavrenov 2013), or rely on analytic approximations. Typically, we solve (4.3)–(4.5), exhibiting $p(\boldsymbol{x}, \boldsymbol{k}\,|\,\boldsymbol{x}_r^0, \boldsymbol{k}_r^0, t)$, the distribution of the ray $(\boldsymbol{x}, \boldsymbol{k})$ at time t given initial conditions $(\boldsymbol{x}_r^0, \boldsymbol{k}^0)$. Then by analogy with tracers in incompressible turbulence (Piterbarg & Ostrovskii 1997, (1.31); see also Appendix D), we can evaluate the wave action spectrum mean – or any pointwise statistics – as

$$\mathbb{E}N(\boldsymbol{x}, \boldsymbol{k}, t) = \iint \mathrm{d}\boldsymbol{x}_r^0\,\mathrm{d}\boldsymbol{k}^0\, N^0(\boldsymbol{x}_r^0, \boldsymbol{k}_r^0)\, p(\boldsymbol{x}, \boldsymbol{k}\,|\,\boldsymbol{x}_r^0, \boldsymbol{k}^0, t), \tag{4.10}$$

where N^0 is the initial wave action spectrum. Integrating this expression over wavevectors, we note that the distribution inside the integrals changes:

$$\mathbb{E}A(\boldsymbol{x}, t) = \iint \mathrm{d}\boldsymbol{x}_r^0\,\mathrm{d}\boldsymbol{k}^0\, N^0(\boldsymbol{x}_r^0, \boldsymbol{k}_r^0)\, p(\boldsymbol{x}\,|\,\boldsymbol{x}_r^0, \boldsymbol{k}^0, t). \tag{4.11}$$

The wave action mean depends solely on group positions distribution. Multi-point action statistics – e.g. focusing $\mathbb{E}\|\nabla_x A\|^2$ – rely on multi-ray correlations, encoded in the stochastic characteristic equations (4.1), but not the simplified model (4.3)–(4.6). Alternatively, Eulerian descriptions of wave action dynamics directly provide action distribution over space and wavevector.

4.2. *Eulerian dynamics and action diffusion*

Wave action spectrum is transported along a four-dimensional volume-preserving stochastic flow (4.1). Again by analogy with incompressible turbulence (Resseguier *et al.*

2017a), the stochastic transport of wave action spectrum in Itō notations reads

$$\partial_t N + \left(\boldsymbol{v}_g^0 + \bar{\boldsymbol{v}} + \boldsymbol{\sigma} \, \frac{\mathrm{d}B_t}{\mathrm{d}t} \right) \cdot \boldsymbol{\nabla}_x N + \left(-\boldsymbol{\nabla}_x \left(\bar{\boldsymbol{v}} + \boldsymbol{\sigma} \, \frac{\mathrm{d}B_t}{\mathrm{d}t} \right)^{\mathrm{T}} \boldsymbol{k} \right) \cdot \boldsymbol{\nabla}_k N$$

$$= \begin{bmatrix} \boldsymbol{\nabla}_x \\ \boldsymbol{\nabla}_k \end{bmatrix} \cdot \left(\boldsymbol{D} \begin{bmatrix} \boldsymbol{\nabla}_x \\ \boldsymbol{\nabla}_k \end{bmatrix} N \right) = \frac{1}{2} a_0 \, \Delta_x N + \frac{1}{2} \gamma_0 \, \frac{1}{k} \, \partial_k \left(k^3 \, \partial_k N \right) + \frac{3}{2} \gamma_0 \, \partial_{\theta_k}^2 N. \quad (4.12)$$

The right-hand side is reminiscent of (3.16) in Bôas & Young (2020), and (36) in Smit & Janssen (2019), and more generally of rapid wave models. Nevertheless, (4.12) is not averaged and explicitly involves large-scale currents and noise terms (terms with factor $\mathrm{d}B_t/\mathrm{d}t$). Differences with Smit & Janssen (2019) and Bôas & Young (2020) for the diffusivity estimates and the detailed computation of the 4×4 diffusion matrix $\boldsymbol{D}$ can be found in Appendix A. Itō notations for (4.12) explicitly separate mean terms (e.g. diffusion terms) and zero-mean noise terms. Here, the Eulerian Itō notations reveal that coefficients $\frac{1}{2} a_0$, $\frac{1}{2} \gamma_0$ and $\frac{3}{2} \gamma_0$ act to diffuse wave action in space, wavenumber and wavevector angle, respectively.

5. Numerical experiments

To illustrate these developments, we consider ocean surface gravity waves propagating over a dynamical flow region. Ray tracing through synthetic surface currents will provide a benchmark. It will be shown that a broad range of the current scales can be replaced by the stochastic parametrization (3.11) without affecting ray scattering and action distribution. Theoretical results (4.3)–(4.12) will suggest approximate analytic solutions.

5.1. *Surface current dynamics*

Simplified upper ocean dynamics are considered to follow

$$(\partial_t + \boldsymbol{v} \cdot \boldsymbol{\nabla})\Theta = 0, \quad \text{with } \boldsymbol{v} = -\boldsymbol{\nabla}^\perp (-\Delta)^{-\xi} \Theta, \quad (5.1)$$

where Θ stands for the buoyancy, $\boldsymbol{\nabla}^\perp$ for the curl, and Δ for the Laplacian. Two extreme cases are the surface quasi-geostrophic (SQG) dynamics ($\xi = \frac{1}{2}$) (Held *et al.* 1995; Lapeyre 2017), and the 2-D Euler dynamics ($\xi = 1$). The SQG dynamics has an extreme locality (kinetic energy spectrum slope $-5/3$), whereas 2-D Euler dynamics has an extreme non-locality (kinetic energy spectrum slope -3). The objective is to test how the proposed closures apply to both dynamics to be equally useful for any more realistic upper ocean dynamics. Additionally, test cases are developed to assess the multiscale stochastic closure in both homogeneous and heterogeneous propagating media. Moreover, we would like to challenge our closure beyond the validity of rapid wave models. In our first test case, surface fast waves travel in a homogeneous and isotropic SQG turbulence. Then we simulate waves propagating in a spatially heterogeneous 2-D Euler turbulence, mimicking an oceanic jet. For both SQG and 2-D Euler dynamics, a reference simulation is obtained at resolution 512×512 for a $1000 \, \mathrm{km}^2$ domain, with the help of a pseudo-spectral code (Resseguier *et al.* 2017b, 2020b). Once initialized, the current velocity $\boldsymbol{v}$ is approximately $0.1 \, \mathrm{m \, s^{-1}}$ for the homogeneous turbulence, and $1 \, \mathrm{m \, s^{-1}}$ for the jet (see figure 3).

(a)

||U||, t = 0 days

(b)

||U||, t = 0 days
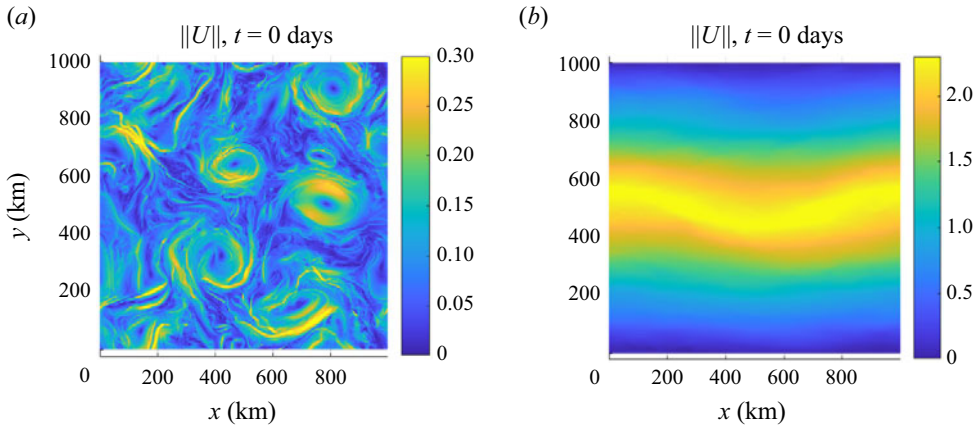
Figure 3. Current velocity norms of (a) the SQG homogeneous turbulence and (b) the 2-D Euler jet current at high resolution (512 × 512).
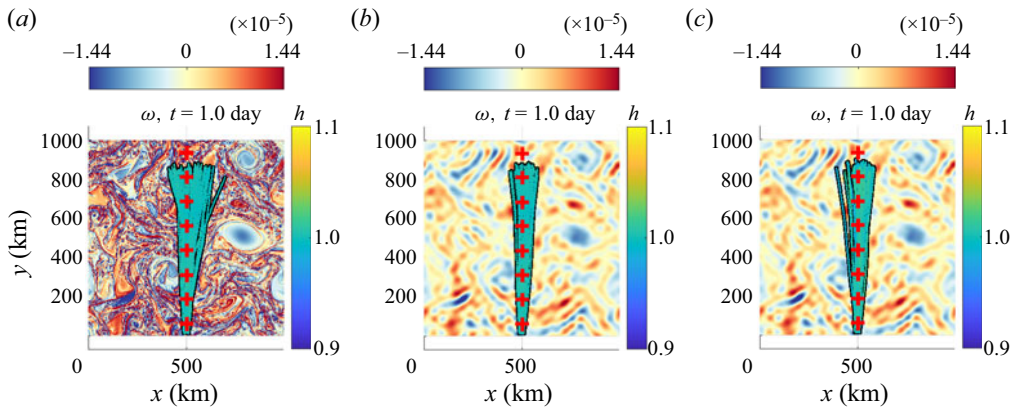
(a)   (b)   (c)

Figure 4. Swell (wavelength $\lambda = 250$ m) interacting with (a) a high-resolution (512 × 512) deterministic SQG current, (b) a low-resolution (32 × 32) deterministic SQG current, and (c) a low-resolution (32 × 32) deterministic SQG current plus (one realization of) the time-uncorrelated stochastic model – coloured by the corresponding wave amplitude, $h(t) = \sqrt{\omega_0(k(t)) N(t = 0)}$ (right-hand side colour bars) – computed by forward advection and superimposed on the current vorticity $\omega = \nabla^\perp \cdot v$. The red crosses indicate where the bidirectional wave spectra of figure 5 are computed.

5.2. *Rays scattering in homogeneous SQG turbulence*

A wave system enters the bottom boundary, propagating to the top. The carrier incident wave has intrinsic wave group velocity $10\,\mathrm{m\,s^{-1}}$, i.e. wavelength $\lambda = 250$ m. Its envelope is Gaussian with isotropic spatial extension 30λ. Figures 4(a) and 5(a) illustrate the resulting dynamics, spreading the wavevectors (figure 5) of the incoming waves. From bottom to top, spectral diffusion occurs (figure 5) in the direction orthogonal (here k_x) to the propagation (here k_y), in line with the additive noise appearing in (4.6). This scattering accelerates – along the propagation – the wave position spread (figure 4). This acceleration is explained by the ray equation (4.3) dominated by the intrinsic wave group velocity.

To mimic a badly resolved $\bar{v}$ field, v is smoothed at resolution 32 × 32. Using this coarse-scale current in figures 4(b) and 5(b), the scattering – described in the previous paragraph – is strongly depleting in comparison to ray tracing in fully-resolved turbulence.
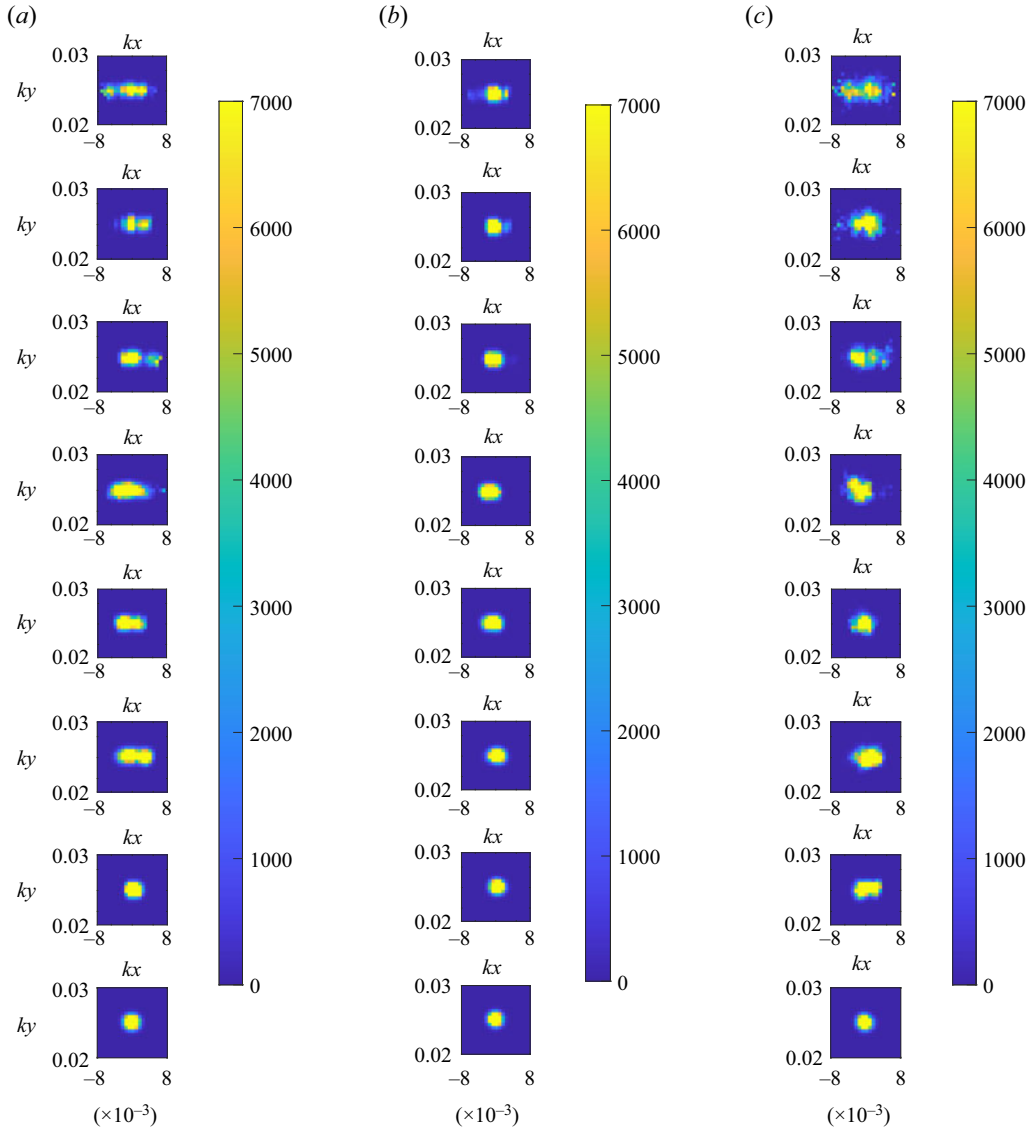
997 A51-11

Figure 5. Bidirectional wave spectra, computed by backward advection, at eight locations along a vertical axis (the mean wave propagation direction) resulting from a swell interacting with (*a*) a high-resolution (512×512) deterministic SQG current, (*b*) a low-resolution (32×32) deterministic SQG current, and (*c*) a low-resolution (32×32) deterministic SQG current plus (one realization of) the stochastic model (3.11). The spatial locations where the spectra are calculated are highlighted in figure 4 by the red crosses.

The spectral diffusion induced by small-scale turbulence is missing. Thus the spatial spreading also is narrower compared to high-resolution simulations. A stochastic current $\boldsymbol{v}'$ is then added for ray tracing (4.1). This stochastic component is divergence-free and has a self-similar distribution of energy across spatial scales (3.11) (see figure 1). The resulting spatial and spectral spreads are now comparable to simulations with high-resolution currents. For this setting, the stochastic closure provides satisfying results for a sufficiently well-resolved large-scale current. The key decorrelation ratio $\epsilon = (l_{v'}/l_v)(\|\boldsymbol{v}\|/v_g^0)$ indeed depends on the resolution through $l_{v'}$. The large-scale current $\bar{\boldsymbol{v}}$ is resolved on a 32×32

997 A51-12

grid, i.e. with resolution $l_{v'} = (\|\boldsymbol{\nabla}\boldsymbol{v}^{\mathrm{T}}\|/\|\boldsymbol{\nabla}\boldsymbol{v}'^{\mathrm{T}}\|)l_v = 0.33l_v$. As such, $\epsilon = 4.1 \times 10^{-3}$, computed with $v_g^0 \approx 10\,\mathrm{m\,s^{-1}}$ and $\|\boldsymbol{v}\| \approx 0.12\,\mathrm{m\,s^{-1}}$, so $\|\boldsymbol{v}\|/v_g^0 \approx 1.2 \times 10^{-2}$, which is sufficiently small to make the proposed model applicable.

From the ADSD estimate (3.10) (illustrated by figure 1) and (4.7)–(4.8), evaluations of the diffusivity coefficients a_0 and γ_0 are straightforward. As discussed previously (Smit & Janssen 2019), the spatial diffusivity is extremely weak: $a_0 = 6.4 \times 10^{-1}\,\mathrm{m^2\,s^{-1}}$ (spatial variations in ray equations (4.3)–(4.4) of approximately $\sqrt{a_0 t} = 230\,\mathrm{m}$ during 1 day). In contrast, the spectral angle diffusivity is large: $3\gamma_0 = 3.0 \times 10^{-8}\,\mathrm{rad^2\,s^{-1}}$. Along our 1-day simulation, neglecting large-scale velocity influence, (4.6) leads to Brownian wavevector angle variations $\delta\theta_k = \theta_k - \theta_k(0) = \sqrt{3\gamma_0}\,B_t^{(4)}$ with standard deviation $\sigma_{\delta\theta_k} = \sqrt{3\gamma_0 t} = 5.2 \times 10^{-2}\,\mathrm{rad} \approx 3.0°$, eventually increasing the wave group spectral maximal extension from $\pm 2\sigma_{k_x} = \pm 2(2\pi/30\lambda) = \pm 1.7 \times 10^{-3}\,\mathrm{rad\,m^{-1}}$ to $\pm 2\sigma_{k_x} \approx \pm 2\sqrt{(2\pi/30\lambda)^2 + (k\sigma_{\delta\theta_k})^2} = \pm 3.1 \times 10^{-3}\,\mathrm{rad\,m^{-1}}$, confirmed by figure 5. This figure also illustrates the wave action diffusion induced by diffusivity γ_0, well predicted by the Eulerian wave action model (4.12). In this scattering regime, the increased angle variability leads, by advection, to a spatial spread. The simplified ray equation (4.3) gives $\delta x \approx \int_0^t v_g^0 \cos\theta_k\,\mathrm{d}t' \approx v_g^0 \int_0^t \delta\theta_k\,\mathrm{d}t' \approx v_g^0\sqrt{3\gamma_0}\int_0^t B_{t'}^{(4)}\,\mathrm{d}t'$ with maximal extension $\pm 2\sigma_x \approx \pm 2v_g^0\sqrt{\gamma_0 t^3} \approx \pm 52\,\mathrm{km}$, in agreement with figure 4. Finally, we estimate a first-order delay along the propagation

$$\delta t = t - (y - y(0))/v_g^0 \approx \int_0^t (1 - \sin\theta_k)\mathrm{d}t' \approx \frac{1}{2}\int_0^t \delta\theta_k^2\,\mathrm{d}t' \approx \frac{3}{2}\gamma_0\int_0^t (B_{t'}^{(4)})^2\,\mathrm{d}t', \quad (5.2)$$

with mean value $\mathbb{E}\delta t = \frac{3}{4}\gamma_0 t^2$.

5.3. *Wave groups trapped in a 2-D Euler turbulent jet*

Tests are now performed for rays travelling in fast and strongly heterogeneous 2-D Euler flows. Classical fast wave models – assuming flows of weak amplitude and often uniform statistics – are expected to fail here. Jets exhibit strong current gradients (e.g. Kudryavtsev *et al.* 2017), creating strong ray focusing and possibly rogue events. Passing through localized spatial structures, caustics can appear, but solely from unrealistically collimated wave trains (White & Fornberg 1998; Heller, Kaplan & Dahlen 2008; Wang *et al.* 2023).

Occurrences strongly reduce for finite directional spread (Slunyaev & Shrira 2023). Here, wave groups are trapped in a jet, but nonlinear wave interactions are neglected. The high-resolution numerical simulations (see figure 6) reveal that even linear wave trains are well trapped in adversarial currents. Freund & Fleischman (2002) observed a similar behaviour for acoustic waves in a three-dimensional turbulent jet. Note that during our simulation, rays cross the domain several times (because of the doubly periodic boundary conditions; see Appendix E for technical details). At the top (resp. bottom) of the jet, the vorticity and thus – at first order – rays curvatures (Dysthe 2001) are negative (resp. positive). Therefore, rays oscillate around the jet. A toy model can explain this behaviour. Following the multiscale stochastic approach (4.3)–(4.6), wave scattering is also taken into account.

For very-coarse-grained (4×4) current $\bar{\boldsymbol{v}}$, oscillation remains, but most of the scattering vanishes, as illustrated by figure 7. Moreover, the curvature of the jet creates artificial wave focusing at $t = 8$ and 10 days. Introducing a time-uncorrelated model (3.11) corrects the resolution issue in figure 8. Figure 9 plots the current ADSD. The current

Figure 6. Rays facing a high-resolution (512×512) deterministic 2-D Euler jet current – coloured by the corresponding wave amplitude $h(t) = \sqrt{\omega_0(k(t)) \, N(t = 0)}$ (right-hand side colour bars) – computed by forward advection and superimposed on the current vorticity $\omega = \nabla^\perp \cdot v$ (top colour bars).
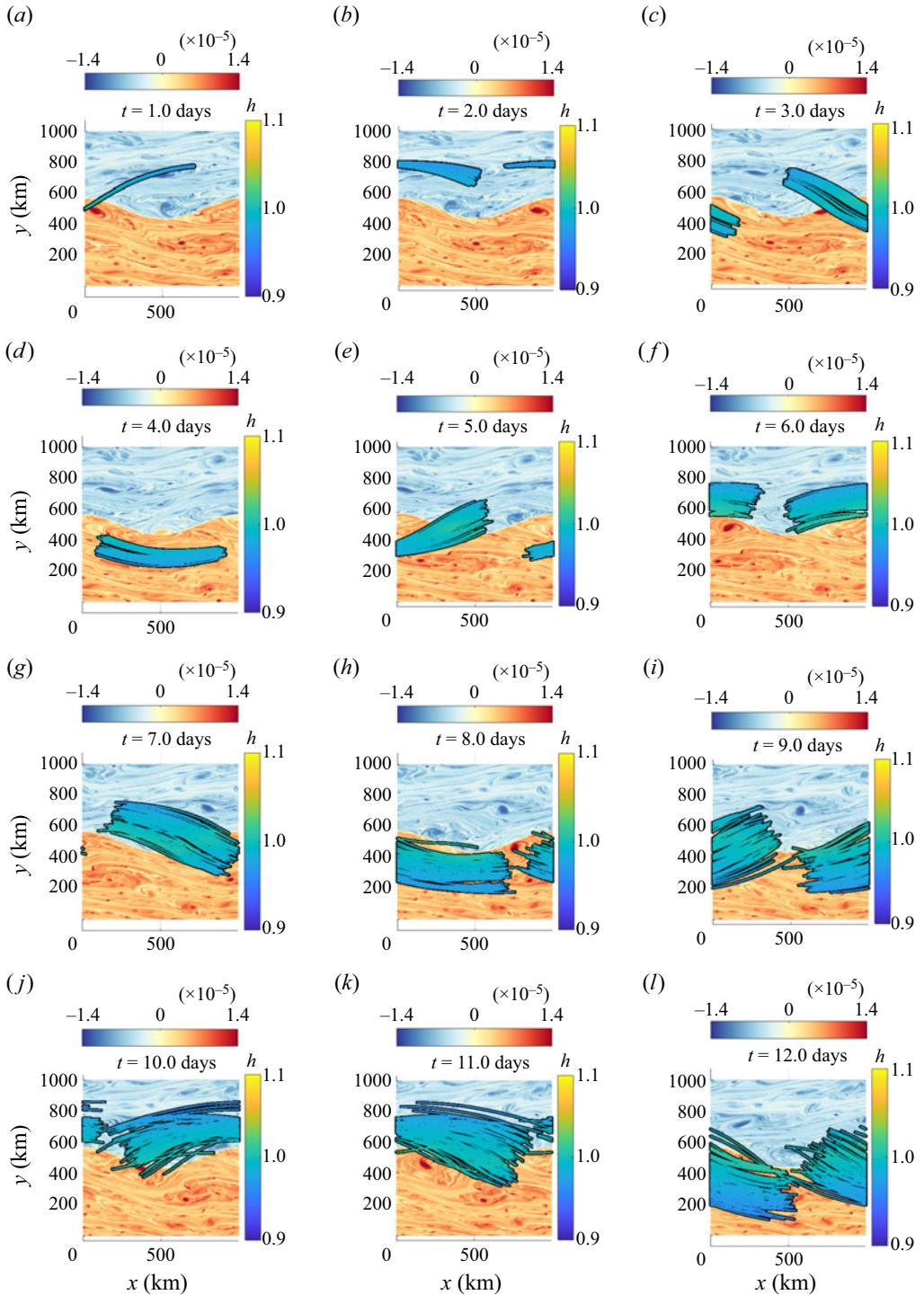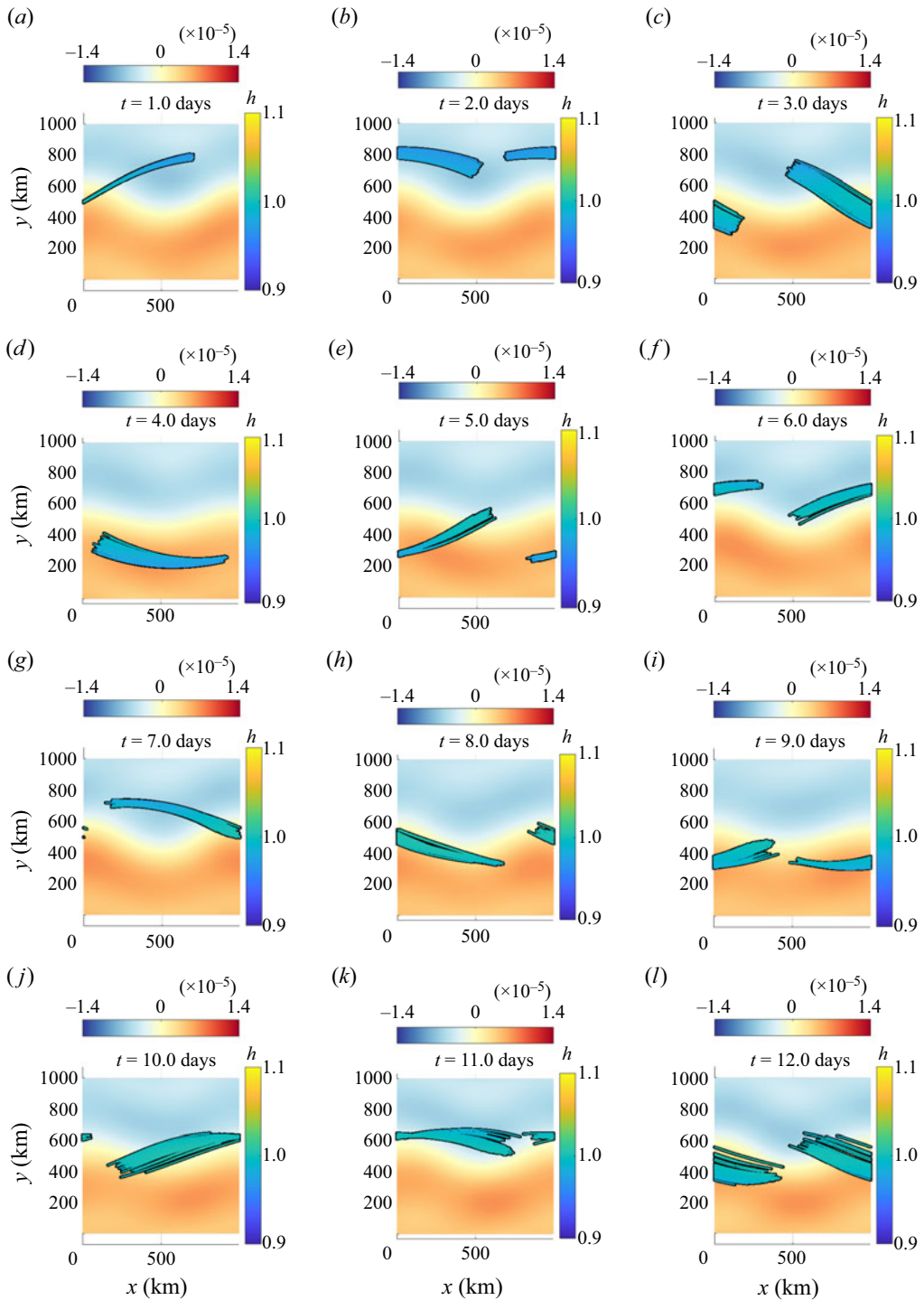
Figure 7. Rays facing a low-resolution (4×4) deterministic 2-D Euler jet current – coloured by the corresponding wave amplitude $h(t) = \sqrt{\omega_0(k(t)) N(t = 0)}$ (right-hand side colour bars) – computed by forward advection and superimposed on the current vorticity $\omega = \nabla^\perp \cdot \boldsymbol{v}$ (top colour bars).

Figure 8. Rays facing a low-resolution (4×4) deterministic 2-D Euler jet current plus (one realization of) the time-uncorrelated stochastic model – coloured by the corresponding wave amplitude $h(t) = \sqrt{\omega_0(k(t)) N(t=0)}$ (right-hand side colour bars) – computed by forward advection and superimposed on the low-resolution current vorticity $\bar{\omega} = \nabla^{\perp} \cdot \bar{v}$ (top colour bars).
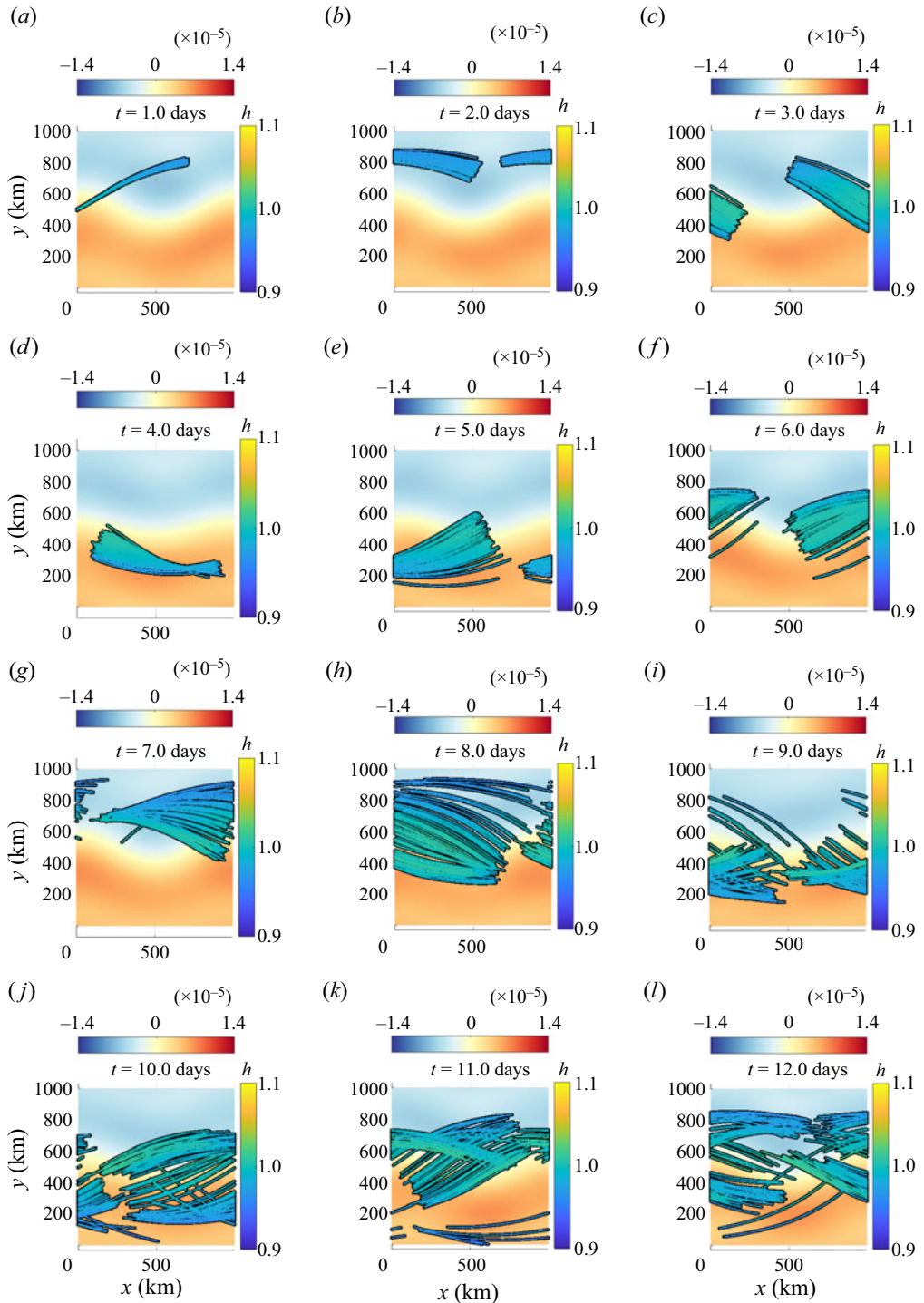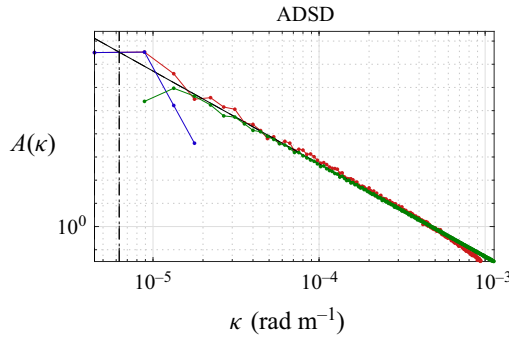
Figure 9. The ADSD ($m^2 s^{-1}/(rad\, m^{-1})$) of the resolved high-resolution jet velocity in red, low-resolution jet velocity in blue, and modelled stochastic velocity in green. The theoretical spectrum slope -3 (black solid line) is imposed, consistent with homogeneous 2-D Euler dynamics. The residual ADSD (green line) is set to extrapolate that power law at small scales.

is strong ($\|\boldsymbol{v}\| \approx 1.4\, m\, s^{-1}$), and the usual fast wave approximation cannot be applied ($\|\boldsymbol{v}\|/v_g^0 \approx 1.2 \times 10^{-1}$). However, the proposed modified fast wave model is valid, even at the very coarse 4×4 resolution.

Indeed, 2-D Euler spectra are steeper than for SQG dynamics, and the length scale ratio is already significant at this resolution, $l_{v'}/l_v = 0.14$, and the derived time-decorrelation ratio is small: $\epsilon = (l_{v'}/l_v)(\|\boldsymbol{v}\|/v_g^0) = 1.6 \times 10^{-2}$.

Furthermore, by approximating the under-resolved current $\bar{v}$, an analytic stochastic solution can be obtained for a ray travelling against the current. The large-scale pattern of the jet takes a quadratic form

$$\bar{u} \approx \bar{U}_0 - \frac{1}{2} \bar{\beta} \left(y - \frac{L_y}{2} \right)^2 \quad \text{and} \quad \bar{v} \approx 0, \quad \text{with } \bar{U}_0, \bar{\beta} < 0. \tag{5.3a,b}$$

Note that the toy model (5.3a,b) simply considers a straight jet, neglecting its curvature. For weak subgrid currents and a ray $(x_r, y'_r + L_y/2, k, \theta_k)$, propagating mainly to the right, θ_k is small and the simplified ray equation (4.4) determines the group position with respect to the jet y'_r:

$$\frac{d}{dt} y'_r \approx v_g^0 \sin(\theta_k) = v_g^0 \theta_k + O(\theta_k^2). \tag{5.4}$$

For frozen turbulence, the wavenumber and hence v_g^0 will not vary significantly. The other ray equation (4.3) localizes the group along the jet, $x_r \approx x_r(0) + (v_g^0 - \bar{u})t$, dropping the $O(\theta_k^2)$ from now on. Moreover, $\tilde{\boldsymbol{k}}^\perp \cdot \nabla \bar{\boldsymbol{v}}^T \tilde{\boldsymbol{k}} \approx -\partial_y \bar{u}$, and the dynamics of wavevector angle (4.6) simplifies to a stochastic oscillator equation:

$$\frac{d^2}{dt^2} y'_r = v_g^0 \frac{d}{dt} \theta_k = s - \partial_y (v_g^0 \bar{u}) + v_g^0 \sqrt{3\gamma_0} \dot{B}_t^{(4)} = -\bar{\omega}_r^2 y'_r + v_g^0 \sqrt{3\gamma_0} \dot{B}_t^{(4)}, \tag{5.5}$$

with $\bar{\omega}_r = \sqrt{|v_g^0 \bar{\beta}|}$. Here, $v_g^0 \bar{u}$ plays the role of a potential, trapping the rays in the jet vicinity, whereas the noise accounts for wave scattering. The solution of this linear
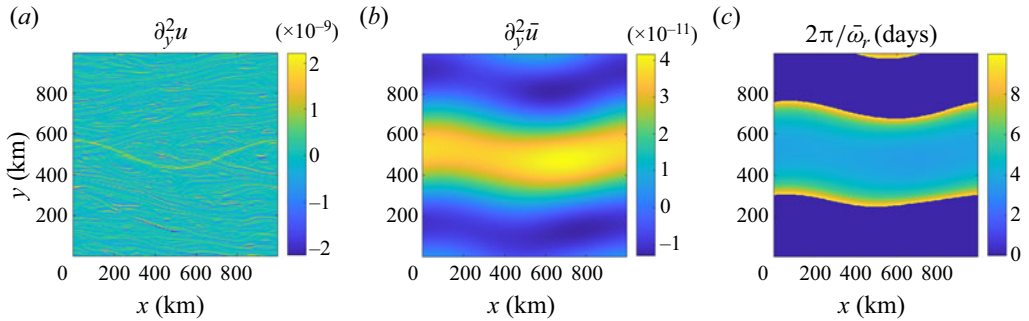
Figure 10. Vorticity shear $\partial_y^2 u$ of the deterministic 2-D Euler jet current at (*a*) high-resolution (512×512) and (*b*) low-resolution (4×4), and (*c*) the corresponding swell system period $2\pi/\bar{\omega}_r$. Far from the jet (± 200 km away), the vorticity shear becomes zero or even positive, so periods larger than 10 days are cropped.

equation is known (e.g. Resseguier *et al.* (2017*a*), (51)–(55)):

$$y_r(t) = \underbrace{\frac{L_y}{2} + y_r'(0)\cos(\bar{\omega}_r t) + \frac{v_g^0}{\bar{\omega}_r}\theta_k(0)\sin(\bar{\omega}_r t)}_{=\,\mathbb{E}(y_r(t))} + \underbrace{Y_{\gamma_0}\sqrt{\bar{\omega}_r}\int_0^t \sin(\bar{\omega}_r(t-r))\,\mathrm{d}B_r^{(4)}}_{=\,y_r''(t)},$$

(5.6)

with $Y_{\gamma_0} = v_g^0\sqrt{3\gamma_0/\bar{\omega}_r^3}$. The wavevector angle solution is similar. The solution ensemble mean $\mathbb{E}y_r$ is a simple coherent deterministic oscillator. This mean solution describes well the interaction between the group and the under-resolved current from figure 7. From the coarse-scale vorticity shear plotted in figure 10 in the vicinity of the jet, we can estimate $\bar{\beta} = -2.7 \times 10^{-11}$ m^{-1} s^{-1}. It yields an oscillation frequency $\bar{\omega}_r = 1.3 \times 10^{-5}$ rad s^{-1}, i.e. period $2\pi/\bar{\omega}_r = 5.7$ days, in agreement with the ray tracing simulations. Note that the high-resolution vorticity shear in figure 10(*a*) does not suggest any relevant values to explain the ray oscillations. Only the proposed multiscale current decomposition provides a quantitative explanation for these oscillations, and by extension for trapping rays inside the jet. Added to the mean solution, the random parts $y_r''(t)$ are continuous summations of zero-mean incoherent wave fluctuations. At each time r, the additive random forcing introduces an oscillation. But the influence of the past excitations is weighed by a sine wave due to the phase change. The group position and wavevector angle are Gaussian random variables (as linear combinations of independent Gaussian variables). Therefore, their finite-dimensional law (i.e. the multi-time probability density function) is entirely defined by their mean and covariance functions. Specifically,

$$\mathbb{E}(y_r''(t)\,y_r''(t+\tau)) = \tfrac{1}{4}Y_{\gamma_0}^2(\cos(\bar{\omega}_r\tau)(2\bar{\omega}_r t - \sin(2\bar{\omega}_r t)) + \sin(\bar{\omega}_r\tau)(1-\cos(2\bar{\omega}_r t))).$$

(5.7)

In particular, the variance of the vertical positions reads $\sigma_y^2(t) = \tfrac{1}{4}Y_{\gamma_0}^2(2\bar{\omega}_r t - \sin(2\bar{\omega}_r t))$. At $t = 2\pi/\bar{\omega}_r$, the group has oscillated once around the jet, and the maximal position extension reaches $\pm 2\sigma_y = \pm 2\sqrt{\pi}\,Y_{\gamma_0} = \pm 42$ km, well confirmed by ray simulations. In contrast, usual fast wave models (e.g. Smit & Janssen 2019) do not consider the interplay between smooth and rough currents, and hence solely predict a classical scattering with a much faster vertical location spreading: $\pm 2\sigma_y = \pm 2\sqrt{(2\pi)^3/3}\,Y_{\gamma_0} = \pm 217$ km. For large time, our multiscale approach predicts a scaling in t, much slower than the usual scattering t^3 scaling.

997 A51-18

From the group vertical location and wavevector angle, we can also solve (4.5) analytically to estimate the group wavenumber variations. For small wavevector angles, $-\int_0^t \bar{\sigma} \sin(\zeta) \, dt' \approx 2\int_0^t \bar{\omega}\theta_k \, dt' = 2\bar{\beta}\int_0^t y_r'\theta_k \, dt'$, and (4.9) together with the analytic solutions for y_r' and θ_k give a closed stochastic expression for the group wavenumber. Thus the wavenumber factor $\exp(2\bar{\beta}\int_0^t y_r'\theta_k \, dt')$ oscillates at frequency $2\bar{\omega}_r$, and the oscillations modulate the wave amplitude: $h = \sqrt{E} = \sqrt{\omega_0 N} = \text{constant} \times k^{1/4}$. The modulations are associated with wave–current energy exchanges (Boury *et al.* 2023), visible in the coloured rays of figures 6, 7 and 8 when the groups enter and exit the jet.

Finally, the conditional ray distribution $p(\boldsymbol{x}, \boldsymbol{k} \,|\, \boldsymbol{x}_r^0, \boldsymbol{k}^0, t)$, the action spectrum mean from (4.10) and the action mean from (4.11) can all be derived. For a system initially localized in $(0, L_y/2)$ with action A^0, wavenumber k^0 and a $\sigma_{\delta\theta_k}^0$-width Gaussian angular spreading, propagating to the right, the action mean reads

$$\mathbb{E}A(x, y, t) = A^0 \delta(x - (v_g^0(k^0) - \bar{u}(y))t) \mathcal{N}\left(y - \frac{L_y}{2} \,\middle|\, \tilde{\sigma}_y^2(t) \right), \qquad (5.8)$$

with $\mathcal{N}(\cdot \,|\, \tilde{\sigma}_y^2(t))$ a Gaussian function with variance $\tilde{\sigma}_y^2(t) = \sigma_y^2(t) + ((v_g^0/\bar{\omega}_r)\sin(\bar{\omega}_r t) \sigma_{\delta\theta_k}^0)^2$. The action is advected in the horizontal direction, and slowly diffuses along the vertical direction.

6. Conclusion

Developed to generalize the ray path concept for waves propagating over a heterogeneous turbulence, a practical stochastic framework is derived. For fast waves, the smallest scales of a turbulent flow decorrelate along the wave propagation. Flows with steeper spectra decorrelate faster, leading to a broader validity range of fast wave approximations. The proposed framework encodes both large-scale refraction and random scattering effects on wave statistical properties. The mean wave action statistics are directly linked to resolved strain rate and vorticity, but also to unresolved kinetic energy spectral properties. Both Eulerian and Lagrangian views are presented. A convenient calibration method is also proposed for the subgrid parametrization.

As anticipated, random horizontal currents delay wave arrival and augment the initial radiative transport equation with a directional diffusive term. These phenomena are illustrated with numerical simulations, analytical solutions and quantitative proxies describing weak homogeneous turbulence. Using these proxies, measured delays in ray arrivals, estimated wave energy spectral characteristics and decays, and/or varying directional spread, will then be more quantitatively interpreted. It will lead to valuable information about underlying flow properties.

The generalized fast wave approximation does takes into account wavenumber variation and handles strong heterogeneous flows, like localized jets with strong current gradients. As compared to numerical simulations, numerical and theoretical results explain and quantify ray trapping effects by jets, unlike usual fast wave approaches.

Among the fast wave literature, isotropic diffusion and hence wavenumber diffusion may (e.g. Voronovich 1991) or may not (e.g. Bôas & Young 2020) come into play (see Appendix C for details). Future works could adapt our convenient stochastic calculus framework to the second models family. Besides, further analytical developments could consider finite-size wave groups, their dynamics (Jonsson 1990; White & Fornberg 1998) and statistical distributions, or alternatively the Eulerian action dynamics (4.12) with all its multi-point stochastic structure. When achieved, this next theoretical development

could provide new means to analyse wave dynamics with subsequent fast simulations of ensembles. Beside comprehension and analysis, our stochastic simulation tools aim to eventually facilitate future ensemble-based data assimilation algorithms (Smit *et al.* 2021).

Declaration of interests. The authors report no conflict of interest.

Data availability statement. SCALIAN DS owns a portion of the developed code intellectual property. For commercial reasons, that code will remain private.

Author ORCID.
 Valentin Resseguier https://orcid.org/0000-0002-9301-9493.

Author contributions. V.R. developed the theory. V.R. and E.H. wrote the code and performed numerical experiments. V.R. and B.C. wrote the paper.

Appendix A. Stochastic forcing covariance

In this Appendix, we will compute the conditional covariance of the stochastic forcing of our eikonal characteristic equations (4.1), i.e.

$$2\boldsymbol{D} \triangleq \frac{1}{\mathrm{d}t}\mathbb{E}_t\left\{\begin{pmatrix}\boldsymbol{\sigma}\,\mathrm{d}B_t\\ \mathrm{d}\boldsymbol{\eta}_t\end{pmatrix}\begin{pmatrix}\boldsymbol{\sigma}\,\mathrm{d}B_t\\ \mathrm{d}\boldsymbol{\eta}_t\end{pmatrix}^{\mathrm{T}}\right\} = \begin{bmatrix}\boldsymbol{a} & \boldsymbol{\Sigma}_{\eta,\sigma}\\ \boldsymbol{\Sigma}_{\eta,\sigma}^{\mathrm{T}} & \boldsymbol{\Sigma}_\eta\end{bmatrix}, \tag{A1}$$

where $\mathrm{d}\boldsymbol{\eta}_t = -\boldsymbol{\nabla}(\boldsymbol{\sigma}\,\mathrm{d}B_t)^{\mathrm{T}}\boldsymbol{k}$ denotes the wavevector stochastic forcing, $\boldsymbol{\Sigma}_\eta\,\mathrm{d}t$ is its covariance, and $\mathbb{E}_t\{\cdot\} \triangleq \mathbb{E}\{\cdot \mid \boldsymbol{x}_r(t), \boldsymbol{k}(t)\}$ stands for the conditional expectation evaluated with given characteristics $(\boldsymbol{x}_r(t), \boldsymbol{k}(t))$ at the current time t. Note that in this Appendix we use Itō notations only.

The subgrid velocity $\boldsymbol{v}' = \boldsymbol{\sigma}\,\mathrm{d}B_t/\mathrm{d}t$ is constructed in Fourier space with a divergence-free isotropic spatial filter $\boldsymbol{\nabla}^\perp\breve{\psi}_\sigma$ (see (3.11)):

$$\widehat{\boldsymbol{v}'}(\boldsymbol{\kappa}, t) = \int \mathrm{d}\boldsymbol{x}\,\boldsymbol{v}'(\boldsymbol{x}, t)\exp(-\mathrm{i}\boldsymbol{\kappa}\cdot\boldsymbol{x}) = \widehat{\boldsymbol{\sigma}\,\mathrm{d}B_t}/\mathrm{d}t(\boldsymbol{\kappa}, t) = \mathrm{i}\boldsymbol{\kappa}^\perp\hat{\breve{\psi}}_\sigma(\kappa)\,\widehat{\mathrm{d}B_t}(\boldsymbol{\kappa})/\mathrm{d}t, \tag{A2}$$

where $\kappa^\perp$ is the vector directly orthogonal to κ. The computation of the variance tensor $\boldsymbol{a}$ is classical and straightforward from the definition of the inverse Fourier transform and the identity $\mathbb{E}\{\widehat{\mathrm{d}B_t}(\boldsymbol{\kappa}_1)\,\widehat{\mathrm{d}B_t}^*(\boldsymbol{\kappa}_2)\} = (2\pi)^2\delta(\boldsymbol{\kappa}_1 - \boldsymbol{\kappa}_2)\,\mathrm{d}t$, where * denotes complex conjugate. We simply need to split the integral of the stochastic forcing spectrum over the current wavevector $\boldsymbol{\kappa} = \kappa(\cos\theta_\kappa, \sin\theta_\kappa)$:

$$\begin{aligned}\boldsymbol{a} &= \frac{1}{(2\pi)^4\,\mathrm{d}t}\iint \mathrm{d}\boldsymbol{\kappa}_1\,\mathrm{d}\boldsymbol{\kappa}_2\,\mathbb{E}_t\left\{(\widehat{\boldsymbol{\sigma}\,\mathrm{d}B_t})(\boldsymbol{\kappa}_1, \boldsymbol{k})\,(\widehat{\boldsymbol{\sigma}\,\mathrm{d}B_t}^{\mathrm{T}})^*(\boldsymbol{\kappa}_2, \boldsymbol{k})\right\}\exp(\mathrm{i}(\boldsymbol{\kappa}_1 - \boldsymbol{\kappa}_2)\cdot\boldsymbol{x})\\ &= \frac{1}{(2\pi)^2}\int \mathrm{d}\boldsymbol{\kappa}\,\kappa^2\,|\hat{\breve{\psi}}_\sigma(\kappa)|^2\begin{pmatrix}-\sin\theta_\kappa\\ \cos\theta_\kappa\end{pmatrix}\begin{pmatrix}-\sin\theta_\kappa\\ \cos\theta_\kappa\end{pmatrix}^{\mathrm{T}}\\ &= \frac{1}{(2\pi)^2}\int_0^{+\infty}\oint_0^{2\pi}\mathrm{d}\kappa\,\mathrm{d}\theta_\kappa\,\kappa^3\,|\hat{\breve{\psi}}_\sigma(\kappa)|^2\begin{bmatrix}\sin^2\theta_\kappa & -\sin\theta_\kappa\cos\theta_\kappa\\ -\sin\theta_\kappa\cos\theta_\kappa & \cos^2\theta_\kappa\end{bmatrix}\end{aligned}$$

$$= \frac{2}{2\pi} a_0 \oint_0^{2\pi} \mathrm{d}\theta_\kappa \begin{bmatrix} \sin^2 \theta_\kappa & -\sin \theta_\kappa \cos \theta_\kappa \\ -\sin \theta_\kappa \cos \theta_\kappa & \cos^2 \theta_\kappa \end{bmatrix}$$

$$= a_0 \mathbb{I}_d, \tag{A3}$$

where a_0 is defined by (4.7).

Now, the Fourier transform of the wavevector stochastic forcing is

$$\mathrm{d}\hat{\boldsymbol{\eta}}_t = -\widehat{\boldsymbol{\nabla}(\boldsymbol{\sigma}\,\mathrm{d}B_t)}^\mathrm{T} \boldsymbol{k} = -\mathrm{i}\boldsymbol{\kappa}(\mathrm{i}\boldsymbol{\kappa}^\perp \hat{\tilde{\psi}}_\sigma \widehat{\mathrm{d}B_t}) \cdot \boldsymbol{k} = \boldsymbol{\kappa}(\boldsymbol{\kappa}^\perp \cdot \boldsymbol{k}) \hat{\tilde{\psi}}_\sigma \widehat{\mathrm{d}B_t} = -\boldsymbol{\kappa}(\boldsymbol{k}^\perp \cdot \boldsymbol{\kappa}) \hat{\tilde{\psi}}_\sigma \widehat{\mathrm{d}B_t}. \tag{A4}$$

Then applying the crest-oriented rotation matrix $\boldsymbol{M}_k = \begin{bmatrix} \tilde{\boldsymbol{k}} & \tilde{\boldsymbol{k}}^\perp \end{bmatrix}$ leads to

$$\mathrm{d}\hat{\boldsymbol{Z}}_t = \boldsymbol{M}_k^\mathrm{T} \mathrm{d}\hat{\boldsymbol{\eta}}_t = -\begin{pmatrix} \tilde{\boldsymbol{k}} \cdot \boldsymbol{\kappa} \\ \tilde{\boldsymbol{k}}^\perp \cdot \boldsymbol{\kappa} \end{pmatrix} (\boldsymbol{k}^\perp \cdot \boldsymbol{\kappa}) \hat{\tilde{\psi}}_\sigma \widehat{\mathrm{d}B_t} = -\begin{pmatrix} \cos \delta\theta \sin \delta\theta \\ \sin^2 \delta\theta \end{pmatrix} \kappa^2 k \hat{\tilde{\psi}}_\sigma \widehat{\mathrm{d}B_t}, \quad \text{(A5)}$$

with $\delta\theta = \theta_\kappa - \theta_k$. From there, we can evaluate the conditional covariance matrix $\boldsymbol{\Sigma}_Z = (1/\mathrm{d}t)\,\mathbb{E}_t\{\mathrm{d}\boldsymbol{Z}_t\,\mathrm{d}\boldsymbol{Z}_t^\mathrm{T}\}$ of $\mathrm{d}\boldsymbol{Z}_t$ as before:

$$\boldsymbol{\Sigma}_Z = \frac{1}{(2\pi)^4\,\mathrm{d}t} \iint \mathrm{d}\boldsymbol{\kappa}_1\,\mathrm{d}\boldsymbol{\kappa}_2\,\mathbb{E}_t\{(\mathrm{d}\hat{\boldsymbol{Z}}_t)(\boldsymbol{\kappa}_1, \boldsymbol{k})\,(\mathrm{d}\hat{\boldsymbol{Z}}_t^\mathrm{T})^*(\boldsymbol{\kappa}_2, \boldsymbol{k})\} \exp(\mathrm{i}(\boldsymbol{\kappa}_1 - \boldsymbol{\kappa}_2) \cdot \boldsymbol{x})$$

$$= \frac{1}{(2\pi)^2} \int_0^{+\infty} \oint_0^{2\pi} \mathrm{d}\kappa\,\mathrm{d}\delta\theta\,\kappa^5 k^2\,|\hat{\tilde{\psi}}_\sigma(\kappa)|^2 \begin{bmatrix} \cos^2 \delta\theta \sin^2 \delta\theta & \cos \delta\theta \sin^3 \delta\theta \\ \cos \delta\theta \sin^3 \delta\theta & \sin^4 \delta\theta \end{bmatrix}$$

$$= \gamma_0 k^2 \begin{bmatrix} 1 & 0 \\ 0 & 3 \end{bmatrix}. \tag{A6}$$

Finally, we come back to the canonical frame to get

$$\boldsymbol{\Sigma}_\eta = \mathbb{E}_t\{\mathrm{d}\boldsymbol{\eta}_t\,\mathrm{d}\boldsymbol{\eta}_t^\mathrm{T}\} = \boldsymbol{M}_k \boldsymbol{\Sigma}_Z \boldsymbol{M}_k^\mathrm{T} = \gamma_0 k^2 [\tilde{\boldsymbol{k}}\tilde{\boldsymbol{k}}^\mathrm{T} + 3\tilde{\boldsymbol{k}}^\perp (\tilde{\boldsymbol{k}}^\perp)^\mathrm{T}]. \tag{A7}$$

For noises cross-correlations, by isotropy, it is also straightforward to show that

$$\boldsymbol{\Sigma}_{\eta,\sigma} = 0. \tag{A8}$$

The stochastic forcings of $\boldsymbol{x}_r$ and $\boldsymbol{k}$ are hence (conditionally) independent from one another.

Appendix B. Single-ray dynamics

The Itō noise $\begin{pmatrix} \boldsymbol{\sigma}\,\mathrm{d}B_t \\ \mathrm{d}\boldsymbol{\eta}_t \end{pmatrix}$ is white in time and conditionally Gaussian. Its conditional single-point distribution is fully determined by its zero mean and its local covariance matrix (given by (A1), (A3), (A7) and (A8)). In particular, we can replace this noise by another zero-mean Gaussian vector with the same covariance without changing the single-ray dynamics – typically replacing $\boldsymbol{\sigma}\,\mathrm{d}B_t$ by $\sqrt{a_0}\begin{pmatrix} \mathrm{d}B_t^{(1)} \\ \mathrm{d}B_t^{(2)} \end{pmatrix}$, and $\mathrm{d}\boldsymbol{Z}_t$ by $-\sqrt{\gamma_0}k\begin{pmatrix} \mathrm{d}B_t^{(3)} \\ \sqrt{3}\,\mathrm{d}B_t^{(4)} \end{pmatrix}$. This yields the simplified ray equations (4.3)–(4.4).

Then note that from the Itō lemma (Oksendal [1998](#)), $\mathrm{d}\tilde{\boldsymbol{k}} = \mathrm{d}\left(\begin{smallmatrix} \cos\theta_k \\ \sin\theta_k \end{smallmatrix}\right) = \tilde{\boldsymbol{k}}^\perp \mathrm{d}\theta_k - \frac{1}{2}\tilde{\boldsymbol{k}} \, \mathrm{d}\langle\theta_k, \theta_k\rangle_t$, where $\langle\cdot, \cdot\rangle_t$ denotes the quadratic covariation. Thus

$$\mathrm{d}\boldsymbol{k} = \mathrm{d}k\,\tilde{\boldsymbol{k}} + k\,\mathrm{d}\tilde{\boldsymbol{k}} + \mathrm{d}\langle k, \tilde{\boldsymbol{k}}\rangle = \left(\mathrm{d}k - \tfrac{1}{2}k\,\mathrm{d}\langle\theta_k, \theta_k\rangle_t\right)\tilde{\boldsymbol{k}} + \left(k\,\mathrm{d}\theta_k + \mathrm{d}\langle k, \theta_k\rangle_t\right)\tilde{\boldsymbol{k}}^\perp. \quad \text{(B1)}$$

Projecting this equation and $\mathrm{d}\boldsymbol{k} = -\boldsymbol{\nabla}\bar{\boldsymbol{v}}^{\mathrm{T}}\boldsymbol{k}\,\mathrm{d}t + \mathrm{d}\boldsymbol{\eta}_t$ on $\tilde{\boldsymbol{k}}$ and $\tilde{\boldsymbol{k}}^\perp$, we have

$$\begin{cases} \mathrm{d}k = -\tilde{\boldsymbol{k}} \cdot \boldsymbol{\nabla}\bar{\boldsymbol{v}}^{\mathrm{T}}\boldsymbol{k}\,\mathrm{d}t + (\mathrm{d}Z_t)_1 + \tfrac{1}{2}k\,\mathrm{d}\langle\theta_k, \theta_k\rangle_t, \\ k\,\mathrm{d}\theta_k = -\tilde{\boldsymbol{k}}^\perp \cdot \boldsymbol{\nabla}\bar{\boldsymbol{v}}^{\mathrm{T}}\boldsymbol{k}\,\mathrm{d}t + (\mathrm{d}Z_t)_2 - \mathrm{d}\langle k, \theta_k\rangle_t, \end{cases} \quad \text{(B2)}$$

$$\begin{cases} \mathrm{d}k = -\tilde{\boldsymbol{k}} \cdot \boldsymbol{\nabla}\bar{\boldsymbol{v}}^{\mathrm{T}}\boldsymbol{k}\,\mathrm{d}t + (\mathrm{d}Z_t)_1 + \tfrac{1}{2}k^{-1}\,\mathrm{d}\langle Z_2, Z_2\rangle_t, \\ \mathrm{d}\theta_k = -\tilde{\boldsymbol{k}}^\perp \cdot \boldsymbol{\nabla}\bar{\boldsymbol{v}}^{\mathrm{T}}\tilde{\boldsymbol{k}}\,\mathrm{d}t + k^{-1}(\mathrm{d}Z_t)_2 + \tfrac{1}{2}k^{-2}\,\mathrm{d}\langle Z_1, Z_2\rangle_t. \end{cases} \quad \text{(B3)}$$

The treatment of the large-scale terms $\tilde{\boldsymbol{k}} \cdot \boldsymbol{\nabla}\bar{\boldsymbol{v}}^{\mathrm{T}}\tilde{\boldsymbol{k}}$ and $\tilde{\boldsymbol{k}}^\perp \cdot \boldsymbol{\nabla}\bar{\boldsymbol{v}}^{\mathrm{T}}\tilde{\boldsymbol{k}}$ is classical. Interested readers can refer to Lapeyre *et al.* ([1999](#)) for details. From the Itō lemma again, $\mathrm{d}\log k = \mathrm{d}k/k - \frac{1}{2}\,\mathrm{d}\langle k, k\rangle_t/k^2$, leading to the simplified wavevector dynamics ([4.5](#))–([4.6](#)).

Appendix C. Subgrid flow anisotropy and comparison with other works

Throughout this paper, we have considered an isotropic model for the stochastic subgrid velocity ([3.11](#)). The isotropic diffusivity matrix $\boldsymbol{a} = a_0\mathbb{I}_d$ is a good illustration of this. In contrast, many authors (e.g. White & Fornberg [1998](#); Smit & Janssen [2019](#); Bôas & Young [2020](#)) assume isotropic and homogeneous turbulence, and obtain anisotropic stochastic subgrid models for $\|\boldsymbol{v}\|/v_g^0 \to 0$. In these approaches, the integral over $\delta\theta$ in diffusivity matrix computations ([A3](#)) and ([A6](#)) involve singular integrations over the direction $\boldsymbol{v}_g^0 = v_g^0\tilde{\boldsymbol{k}}$. This makes a Dirac delta function appear: $2\pi\delta(\boldsymbol{\kappa} \cdot \boldsymbol{v}_g^0) = (2\pi/\kappa v_g^0)(\delta(\theta_\kappa - \theta_k - \pi/2) + \delta(\theta_\kappa - \theta_k + \pi/2))$ (see the Appendix in Bôas & Young [2020](#)). This precision imposes a statistical anisotropy for $\boldsymbol{\sigma}\,\mathrm{d}B_t$ (oriented along $\boldsymbol{k}$) and $d\boldsymbol{\eta}_t$ (oriented along $\boldsymbol{k}^\perp$), eventually leading to a covariance $\boldsymbol{\Sigma}_Z = \gamma_0 k^2 \left[\begin{smallmatrix} 0 & 0 \\ 0 & 16 \end{smallmatrix}\right]$ (([3.17](#)) in Bôas & Young ([2020](#)), and (24) in Smit & Janssen ([2019](#))), no noise $\mathrm{d}Z_1$, and no Brownian motion $B_t^{(3)}$. Moreover, because of the scaling assumption, Bôas & Young ([2020](#)) neglect the spatial diffusivity matrix $\boldsymbol{a}$, while Smit & Janssen ([2019](#), (22)–(23)) find $\boldsymbol{a} = 4a_0(\mathbb{I}_d + \frac{5}{4}\tilde{\boldsymbol{k}}\tilde{\boldsymbol{k}}^{\mathrm{T}})$. In this anisotropic framework, the Stratonovich wavevector equation ([2.3](#)), $\mathrm{d}\boldsymbol{k} = -\boldsymbol{\nabla}(\bar{\boldsymbol{v}}\,\mathrm{d}t + \boldsymbol{\sigma} \circ \mathrm{d}B_t)^{\mathrm{T}}\boldsymbol{k}$, would involve an additional drift term in Itō notation.

Further developing this anisotropic stochastic closure is an interesting avenue. A multiscale anisotropic stochastic closure would involve wavenumber variations but no wavenumber diffusion. Nevertheless, in the present study, we adopt the isotropic model for $\boldsymbol{\sigma}\,\mathrm{d}B_t$, which is much more convenient for multi-ray numerical simulations.

Appendix D. Action spectra and ray distribution

Here, we highlight the link between mean action spectral density and the ray distribution. We denote by N^0 the initial wave action spectrum. We first use the definition of the Dirac measure, then perform a variable change corresponding to the characteristic ([2.5](#)) from

$t = t_i$ to $t = t_f$:

$$\mathbb{E}N(\boldsymbol{x}, \boldsymbol{k}, t) = \mathbb{E} \iint \mathrm{d}\boldsymbol{x}_r \, \mathrm{d}\boldsymbol{k}_r \, N(\boldsymbol{x}_r, \boldsymbol{k}_r, t) \, \delta(\boldsymbol{x}_r - \boldsymbol{x}) \, \delta(\boldsymbol{k}_r - \boldsymbol{k})$$

$$= \mathbb{E} \iint \mathrm{d}\boldsymbol{x}_r^0 \, \mathrm{d}\boldsymbol{k}_r^0 \, N(\boldsymbol{x}_r^0, \boldsymbol{k}_r^0, 0) \, \delta(\boldsymbol{x}_r(\boldsymbol{x}_r^0, \boldsymbol{k}_r^0, t) - \boldsymbol{x}) \, \delta(\boldsymbol{k}_r(\boldsymbol{x}_r^0, \boldsymbol{k}_r^0, t) - \boldsymbol{k})$$

$$= \iint \mathrm{d}\boldsymbol{x}_r^0 \, \mathrm{d}\boldsymbol{k}_r^0 \, N^0(\boldsymbol{x}_r^0, \boldsymbol{k}_r^0) \, p(\boldsymbol{x}, \boldsymbol{k} \,|\, \boldsymbol{x}_r^0, \boldsymbol{k}_r^0, t), \tag{D1}$$

where the standard relation between the Dirac measure and the probability distribution function has been used.

Appendix E. Jet simulation

Again, currents are simulated at resolution 512×512 on a $1000\,\mathrm{km}$ width squared domain $[0, L_x] \times [0, L_y]$ through the same code. A backward velocity v_{Bk} forces a leftward jet structure:

$$\partial_t \omega + \boldsymbol{v} \cdot \boldsymbol{\nabla} \omega = S_\omega, \quad \text{with } \boldsymbol{v} = \boldsymbol{\nabla}^\perp \Delta^{-1}(\omega + \omega_{Bk}). \tag{E1}$$

Here, S_ω encompasses the linear drag and the hyperviscosity with coefficient $1/\tau_F = 3.22 \times 10^{-8}\,\mathrm{s}^{-1}$ and $\nu_{HV}/\mathrm{d}x^8 = 3.33 \times 10^{-9}\,\mathrm{s}^{-1}$, respectively. The background vorticity ω_{Bk} is a smooth step function with a wavy interface at $y = Y_{Bk}(x)$:

$$\omega_{Bk}(x, y) = \Omega_{Bk} \left(\frac{1}{2} - \mathrm{erf}\left(\frac{y - Y_{Bk}(x)}{L_y^\omega} \right) \right), \quad \text{with } Y_{Bk}(x) = L_y \left(\frac{1}{2} + \frac{1}{30} \cos\left(\frac{2\pi}{L_x} x \right) \right). \tag{E2}$$

To better highlight the interplay between ray oscillations and scattering, we consider very collimated swells, with spatial extension $100\lambda = 25\,\mathrm{km}$.

Besides, the curvature of the simulated jet can force an additional faster oscillation around the jet for small enough wavevector angle. Indeed, a wave group travelling exactly rightward would cross an alternation of positive and negative vorticity regions with period $L_x/(v_g^0 - \bar{U}_0) \approx 1\,\mathrm{day} < 2\pi/\bar{\omega}_r$. Here, we set an initial wavevector angle large enough to prevent the additional harmonics.

REFERENCES

BAL, G. & CHOU, T. 2002 Capillary–gravity wave transport over spatially random drift. *Wave Motion* **35** (2), 107–124.

BAUER, W., CHANDRAMOULI, P., CHAPRON, B., LI, L. & MÉMIN, E. 2020 Deciphering the role of small-scale inhomogeneity on geophysical flow structuration: a stochastic approach. *J. Phys. Oceanogr.* **50** (4), 983–1003.

BÔAS, A.B.V. & YOUNG, W.R. 2020 Directional diffusion of surface gravity wave action by ocean macroturbulence. *J. Fluid Mech.* **890**, R3.

BORCEA, L., GARNIER, J. & SOLNA, K. 2019 Wave propagation and imaging in moving random media. *Multiscale Model. Simul.* **17** (1), 31–67.

BOURY, S., BÜHLER, O. & SHATAH, J. 2023 Fast–slow wave transitions induced by a random mean flow. *Phys. Rev.* E **108** (5), 055101.

BÜHLER, O. 2009 *Waves and Mean Flows*. Cambridge University Press.

COTTER, C.J., GOTTWALD, G.A. & HOLM, D.D. 2017 Stochastic partial differential fluid equations as a diffusive limit of deterministic Lagrangian multi-time dynamics. *Proc. R. Soc.* A **473** (2205), 20170388.

COX, M.R., KAFIABAD, H.A. & VANNESTE, J. 2023 Inertia-gravity-wave diffusion by geostrophic turbulence: the impact of flow time dependence. *J. Fluid Mech.* **958**, A21.

CRISAN, D. & HOLM, D.D. 2018 Wave breaking for the stochastic Camassa–Holm equation. *Physica* D **376**, 138–143.

DINVAY, E. & MÉMIN, E. 2022 Hamiltonian formulation of the stochastic surface wave problem. *Proc. R. Soc.* A **478** (2265), 20220050.

DONG, W., BÜHLER, O. & SMITH, K.S. 2020 Frequency diffusion of waves by unsteady flows. *J. Fluid Mech.* **905**, R3.

DYSTHE, K.B. 2001 Refraction of gravity waves by weak current gradients. *J. Fluid Mech.* **442**, 157–159.

FREUND, J.B. & FLEISCHMAN, T.G. 2002 Ray traces through unsteady jet turbulence. *Intl J. Aeroacoust.* **1** (1), 83–96.

GARNIER, J., GAY, E. & SAVIN, E. 2020 Multiscale analysis of spectral broadening of acoustic waves by a turbulent shear layer. *Multiscale Model. Simul.* **18** (2), 798–823.

HELD, I., PIERREHUMBERT, R., GARNER, S. & SWANSON, K. 1995 Surface quasi-geostrophic dynamics. *J. Fluid Mech.* **282**, 1–20.

HELL, M.C., FOX-KEMPER, B. & CHAPRON, B. An efficient wave model for surface wave growth and propagation in coupled climate models. *J. Adv. Model. Earth Syst.* (submitted).

HELLER, E.J., KAPLAN, L. & DAHLEN, A. 2008 Refraction of a Gaussian seaway. *J. Geophys. Res.* **113** (C9).

HOLM, D. 2015 Variational principles for stochastic fluid dynamics. *Proc. R. Soc. Lond.* A **471** (2176), 20140963.

HOLM, D.D. 2021 Stochastic variational formulations of fluid wave–current interaction. *J. Nonlinear Sci.* **31** (1), 4.

HOLM, D.D., HU, R. & STREET, O.D. 2023 On the interactions between mean flows and inertial gravity waves. arXiv:2302.04838.

HOLM, D.D. & LUESINK, E. 2021 Stochastic wave–current interaction in thermal shallow water dynamics. *J. Nonlinear Sci.* **31**, 1–56.

JONSSON, I.G. 1990 Wave–current interactions. *The Sea* **9**, 65–120.

KAFIABAD, H.A., SAVVA, M.A.C. & VANNESTE, J. 2019 Diffusion of inertia-gravity waves by geostrophic turbulence. *J. Fluid Mech.* **869**, R7.

KLYATSKIN, V. 2005 *Stochastic Equations through the Eye of the Physicist: Basic Concepts, Exact Results and Asymptotic Approximations*. Elsevier.

KLYATSKIN, V.I. & KOSHEL, K.V. 2015 Anomalous sea surface structures as an object of statistical topography. *Phys. Rev.* E **91** (6), 063003.

KUDRYAVTSEV, V., YUROVSKAYA, M., CHAPRON, B., COLLARD, F. & DONLON, C. 2017 Sun glitter imagery of ocean surface waves. Part 1. Directional spectrum retrieval and validation. *J. Geophys. Res.* **122** (2), 1369–1383.

KUNITA, H. 1997 *Stochastic Flows and Stochastic Differential Equations*. Cambridge University Press.

LANDAU, L.D. & LIFSHITZ, E.M. 1960 *Mechanics*, vol. 1SEP. CUP Archive.

LAPEYRE, G. 2017 Surface quasi-geostrophy. *Fluids* **2** (1), 7.

LAPEYRE, G., KLEIN, P. & HUA, B. 1999 Does the tracer gradient vector align with the strain eigenvectors in 2D turbulence? *Phys. Fluids* **11** (12), 3729–3737.

LAVRENOV, I. 2013 *Wind-Waves in Oceans: Dynamics and Numerical Simulations*. Springer Science and Business Media.

MCCOMAS, C.H. & BRETHERTON, F.P. 1977 Resonant interaction of oceanic internal waves. *J. Geophys. Res.* **82** (9), 1397–1412.

MÉMIN, E. 2014 Fluid flow dynamics under location uncertainty. *Geophys. Astrophys. Fluid Dyn.* **108** (2), 119–146.

MÉMIN, E., LI, L., LAHAYE, N., TISSOT, G. & CHAPRON, B. 2022 Linear wave solutions of a stochastic shallow water model. In *Stochastic Transport in Upper Ocean Dynamics Annual Workshop*, pp. 223–245. Springer Nature.

MIKULEVICIUS, R. & ROZOVSKII, B. 2004 Stochastic Navier–Stokes equations for turbulent flows. *SIAM J. Math. Anal.* **35** (5), 1250–1310.

OKSENDAL, B. 1998 *Stochastic Differential Equations*. Spinger.

PAPANICOLAOU, G. & KOHLER, W. 1974 Asymptotic theory of mixing stochastic ordinary differential equations. *Commun. Pure Appl. Maths* **27** (5), 641–668.

PITERBARG, L. & OSTROVSKII, A. 1997 *Advection and Diffusion in Random Media: Implications for Sea Surface Temperature Anomalies*. Kluwer Academic.

PLOUGONVEN, R. & ZHANG, F. 2014 Internal gravity waves from atmospheric jets and fronts. *Rev. Geophys.* **52** (1), 33–76.

RESSEGUIER, V., LI, L., JOUAN, G., DÉRIAN, P., MÉMIN, E. & BERTRAND, C. 2020*a* New trends in ensemble forecast strategy: uncertainty quantification for coarse-grid computational fluid dynamics. *Arch. Comput. Meth. Engng* **28**, 1–82.

RESSEGUIER, V., MÉMIN, E. & CHAPRON, B. 2017*a* Geophysical flows under location uncertainty. Part 1. Random transport and general models. *Geophys. Astrophys. Fluid Dyn.* **111** (3), 149–176.

RESSEGUIER, V., MÉMIN, E. & CHAPRON, B. 2017*b* Geophysical flows under location uncertainty. Part 2. Quasi-geostrophy and efficient ensemble spreading. *Geophys. Astrophys. Fluid Dyn.* **111** (3), 177–208.

RESSEGUIER, V., PAN, W. & FOX-KEMPER, B. 2020*b* Data-driven versus self-similar parameterizations for stochastic advection by Lie transport and location uncertainty. *Nonlinear Process. Geophys.* **27** (2), 209–234.

SLUNYAEV, A.V. & SHRIRA, V.I. 2023 Extreme dynamics of wave groups on jet currents. *Phys. Fluids* **35** (12), 126606.

SMIT, P.B., HOUGHTON, I.A., JORDANOVA, K., PORTWOOD, T., SHAPIRO, E., CLARK, D., SOSA, M. & JANSSEN, T.T. 2021 Assimilation of significant wave height from distributed ocean wave sensors. *Ocean Model.* **159**, 101738.

SMIT, P.B. & JANSSEN, T.T. 2019 Swell propagation through submesoscale turbulence. *J. Phys. Oceanogr.* **49** (10), 2615–2630.

VORONOVICH, A. 1991 The effect of shortening of waves on random currents. In *Proceedings of Nonlinear Water Waves*.

WANG, H., BÔAS, A.B.V., YOUNG, W.R. & VANNESTE, J. 2023 Scattering of swell by currents. arXiv:2305.12163.

WEST, B.J. 1978 Ray paths in a fluctuating environment. *Phys. Rev.* A **18** (4), 1646.

WHITE, B.S. 1999 Wave action on currents with vorticity. *J. Fluid Mech.* **386**, 329–344.

WHITE, B.S. & FORNBERG, B. 1998 On the chance of freak waves at sea. *J. Fluid Mech.* **355**, 113–138.

ZHEN, Y., RESSEGUIER, V. & CHAPRON, B. 2023 Physically constrained covariance inflation from location uncertainty. *EGUsphere* **2023**, 1.